Department of Complexity and Engineering
Graduate School of Frontier science
The University of Tokyo

2020
Master's Thesis

探査機から受信する電波のスペクトル解析による太陽コロナの研究
Study on the solar corona by spectral analysis of radio waves received from a spacecraft

Submitted Junuary 26, 2021

Supervisor:　Professer Takeshi Imamura

千葉 翔太
Shota Chiba

Abstract

The solar wind is the supersonic plasma (sound speed ~100 km/s) streamed from the corona, which is an outer atmosphere of the sun, and there are two types of the solar wind called the fast wind (~750 km/s) and the slow wind (~300 km/s). It is also known that the solar wind is accelerated rapidly in the outer corona about 5–10 R_S (= solar radii). The coronal heating by magnetohydrodynamic waves and the wave-induced magnetic pressure are thought to play major roles in this rapid acceleration. However, confirmation by observations has been insufficient because physical properties of the solar wind acceleration region, whose plasma is thin and dark, are difficult to observe by optical methods.

In radio occultation observations, coronal plasma disturbs received radio wave's amplitudes and frequency from which we can derive physical parameters such as the flow speed and wave's amplitudes. In this research, we analyze data taken in JAXA's Venus orbiter Akatsuki's radio occultation observations carried out during the superior conjunction periods from May 30, 2016 to June 15, 2016 as well as the observations in 2011. Solar offset distances of about 2 to 10 R_S were probed intermittently 11 times.

Physical parameters (flow velocity, power-law exponent, axial ratio, inner scale, and the magnitude of the power) were retrieved from the intensity scintillation time series by fitting a theoretical spectrum to the observed power spectra. The radial distribution of the derived solar wind velocity clearly showed a difference between the two types of the solar wind. We also found that the inner scale increases with the heliocentric distance and that the fast solar wind has larger inner scales than the slow solar wind. This behavior is consistent with the theoretical model (the inertial length model) both qualitatively and quantitatively.

We applied wavelet analysis to the frequency time series to detect quasi-periodic fluctuations (QPC), that are thought to represent acoustic waves, and quantify the amplitude, the period, and the coherence time of each wave event. The density amplitude and the wave energy flux were also estimated following the method of Miyamoto et al. (2014). We confirmed that the fractional density amplitudes increase with distance up to ~6 R_S. The amplitude reaches tens of percent, suggesting a possibility of wave breaking. The energy fluxes increase with distance up to ~6 R_S, suggesting local generation of waves. It is probable that these radial distributions indicate that the Alfvén waves propagating from the photosphere generate acoustic waves in the outer corona, and the generated acoustic waves dissipate to heat the corona, as suggested by Miyamoto et al. (2014). Furthermore, the energy fluxes in the fast solar wind were larger than the slow wind. The results suggest that the fast solar wind originating from the coronal hole is powered by a larger injection of wave energy than the slow wind originating from other regions.

要旨

太陽風は太陽コロナを起源とする超音速のプラズマ（音速 ~100 km/s)で，速度の違いから高速風(~750 km/s)，低速風(~350 km/s)の二種類に分けられる．また，太陽風はおよそ5 から 10 太陽半径という遠方のコロナで急激に加速されており，この急激な加速には太陽表面からコロナ中を外向きに伝搬する電磁流体波動がコロナを加熱し生じる圧力勾配や磁気圧の勾配が重要な役割を果たしていると考えられているが，太陽風が加速されるような領域では，プラズマが希薄で暗く光学観測を行うのが難しいため，観測による検証が不十分である．電波掩蔽観測はこの太陽風の加速領域を網羅的に観測できるほぼ唯一の観測手段である．

電波掩蔽観測は地球から見て太陽の反対側を通過する際に探査機から送信された電波を通過する太陽風中のプラズマ密度濃淡によって生じる地上局での受信信号の強度変動，周波数変動から太陽風の速度や波動の振幅などの物理量を推定できる．本研究では，2016 年の 5 月 30 日から 6 月 15 の期間で JAXA の金星探査機あかつきが地球から見て太陽の反対側を通過する際に行われた電波掩蔽観測から得られた掩蔽データを用いて解析を行った．2016 年の観測ではおよそ 2 から 10 太陽半径の領域を観測し，11 回に分けて計測が行われた．解析には地上局で受信された周波数変動と強度変動の時系列データを用いた．

我々は受信電波の強度変動のパワースペクトルから太陽風速度，密度変動スペクトルの傾き，乱流が散逸するスケールを示す inner scale 動径分布を推定した．我々の解析によって得られた太陽風速度と同時期に行われた惑星間空間シンチレーション観測によって得られた太陽風速度との比較から，今回の観測では，コロナホール起源と考えられる太陽風（高速風）とそうでない領域を起源とする太陽風（低い速風）を捉えたことが分かった．また，得られた inner scale は距離とともに増加し，コロナホール起源の太陽風はそうでない太陽風より大きな inner scale を持つことを確かめ，この挙動が理論モデル(the inertial length model)と整合していることを示した．

周波数変動の時系列データについては，wavelet 解析を行うことで音波に伴った密度揺らぎと考えられる準周期的な密度変動を検出し，検出した音波の周期，振幅，継続時間を導出した．さらに，Miyamoto et al. (2014) の手法に倣い，検出した音波の密度振幅とエネルギー流束の距離依存性を導出した．背景の大気に対する相対的な密度変動が距離とともに増加し~6 太陽半径という遠方で 1 に近づき，エネルギー流束が~6 太陽半径あたりまで距離とともに増加することから，2011 年に行われた金星探査機あかつきによる電波掩蔽観測の観測結果と同様に，太陽表面から伝播した Alfvén 波に由来の音波が遠方で砕波し，コロナの外層でもエネルギーが注入されていることを示唆した．また，~4 太陽半径あたりでコロナホール起源の太陽風がそうでない太陽風に比べ大きなエネルギー流束を持つことからコロナホール起源の太陽風ではコロナ中でより大きなエネルギーの注入があることを示した．

Contents

1. Introduction

1.1. Acceleration of the solar wind

The solar corona, an outer atmosphere of the sun composed of thin plasma, is as hot as 1 to 2 million K in contrast to the photosphere of about 6000 K. Due to the pressure gradient caused by the high temperature, the supersonic plasma "solar wind" (sound speed ~100 km/s) originates from the corona. The solar wind blows through the interplanetary space and affects the environments of the Earth and other planets.

It is also known that the solar wind is accelerated rapidly from the distance to the Sun's center (heliocentric distance) of several R_S (= solar radii) to ~20 R_S (Fig. 1). The acceleration of the solar wind has been observed by Interplanetary Scintillation (IPS) observations, which uses radio waves emitted from natural radio sources and received by ground stations (e.g., Woo and Armstrong 1981; Scott et al. 1983; Tokumaru et al. 1991, 1995; Coles 1995). Various theoretical models about the acceleration have been proposed since the pioneering work by Parker about half a century ago (Parker 1959). The models suggest that the thermal pressure gradient caused by the coronal high temperatures and the magnetic pressure gradient originating from magnetohydrodynamic waves (Alfvén wave) propagating along radial magnetic fields lead to the solar wind acceleration. However, the mechanism of the heating and the acceleration that continuously occur from the vicinity of the Sun to ~20 R_S has still been unclear and is thought to be one of the major problems in astrophysics (Cranmer et al. 2019).

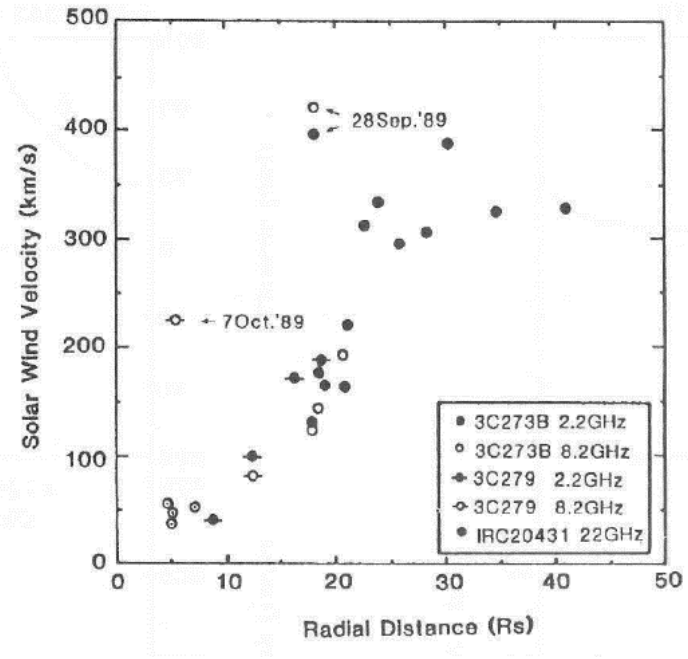

Figure 1. Heliocentric distance of the solar wind velocity measured by IPS observations (Tokumaru et al. 1991).

A possible mechanism of the solar wind acceleration is the wave/turbulence driven model that energy is transferred from the photosphere to the corona by Alfvén waves propagating along radial magnetic fields (e.g., Cranmer 2012); the scenario has been reproduced in magnetohydrodynamics (MHD) simulations (e.g., Suzuki and Inutsuka 2005; Matsumoto and Suzuki 2012; Shoda et al. 2019). In this mechanism, Alfvén waves are excited by the movements of magnetic field lines embedded in photospheric convection cells and propagate outward along magnetic fields. The Alfvén waves generate acoustic waves through nonlinear processes in distant regions and are reflected inward by the acoustic waves. Then, turbulence is generated by the superposition of inward and outward Alfvén waves. The corona is heated by dissipations of turbulence and acoustic waves, leading to the acceleration of the solar wind.

The two-dimensional coronal model by Matsumoto and Suzuki (2012), which successfully reproduced the solar wind, shows density fluctuations generated from Alfvén waves mainly at distances farther than ~3 R_S (Figure 2). The three-dimensional model by Shoda et al. (2019) reproduced radial distributions of outward and inward Elsässer variables, which correspond to outward and inward Alfvén waves, respectively, in the linear regime; Figure 3 indicates reflected Alfvén waves have finer transverse structures like turbulence than

outward Alfvén waves around 4–10 R_S.

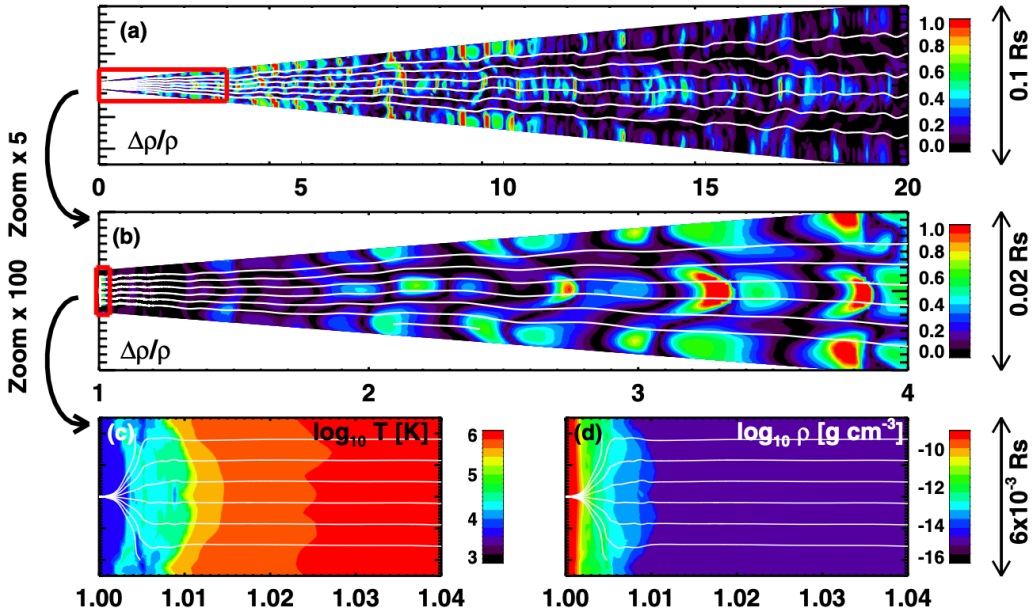

Figure 2. Density fluctuations originating from Alfvén waves reproduced by a MHD simulation (Matsumoto and Suzuki 2012). (a) Normalized density fluctuation and (b) region that is magnified five times. The red squared region in (a) is equivalent to (b). (c) Temperature distribution and (d) density distribution; the regions shown are magnified 100 times from (b).

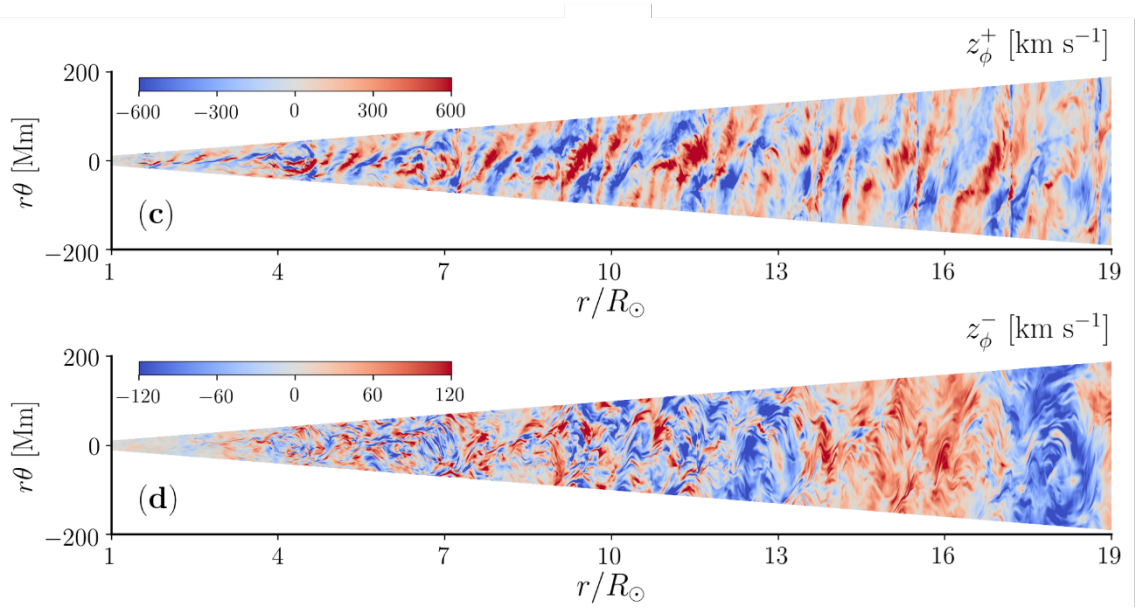

Figure 3. Radial distributions of (upper) outward and (lower) inward Sunward Elsässer variables reproduced by a MHD simulation (Shoda et al. 2019).

As can be seen in these numerical simulations, acoustic waves that are represented by density fluctuations are excited in the outer corona and play an important role in the dissipation of Alfvén waves. For the confirmation of the theory, the distributions of waves and turbulence and the associated solar wind acceleration need to be observed. However, the major acceleration region (2–10 R_S) is too close to the sun for in-situ measurements and too tenuous for optical methods to observe key processes. For these reasons, confirmation by observations has been insufficient. Radio occultation is one of the limited means to observe the acceleration region.

It is also known that there are two types of the solar wind called the fast wind (~750 km/s) and the slow wind (~300 km/s) (e.g., McComas et al. 2008). The fast wind originates from coronal holes where open magnetic fields dominate, and the slow wind originates from the boundary between coronal holes and closed field regions. The fast wind is known to have lower densities than the slow wind. The distribution of the fast and slow solar winds changes during the solar activity cycle with a period of about 11 years. For example, the slow wind is superior during the solar maximum, while in the solar minimum, the slow wind dominates at low latitudes and the fast wind streams from coronal holes at high latitudes. What makes the difference in the flow speed between the fast wind and the slow wind is still unclear; to clarify the key processes causing this difference, it is necessary to compare between the fast and slow winds the radial distributions of wave's amplitude, period, and energy flux, and

turbulence, which will play roles in coronal heating. Moreover, by focusing on the difference of physical processes between the fast winds and slow winds, we can obtain clues to the mechanism of the solar wind acceleration.

1.2. Radio occultation observation

The solar wind velocity has been derived from the power spectra of the intensity scintillations of radio waves emitted by natural radio sources and received at ground stations (Interplanetary scintillation, IPS) (e.g., Woo and Armstrong 1981; Scott et al.1983; Tokumaru et al. 1991, 1995; Coles 1995). In this method, the drift of the diffraction pattern at the ground due to the radial drift of the turbulent density structure is observed as the intensity fluctuation at the ground station, so the flow speed and the information on the turbulence can be obtained from the power spectrum of the scintillation (e.g., Scott et al.1983). Radio occultation observations of the solar corona were conducted also using spacecraft radio signals. During the passage of a spacecraft on the opposite side of the sun as seen from the Earth, radio waves transmitted from the spacecraft are received at the ground station (Figure 4). Coronal plasma disturbs radio wave's amplitude and frequency, from which we can derive various physical parameters such as the flow speed and the wave amplitude.

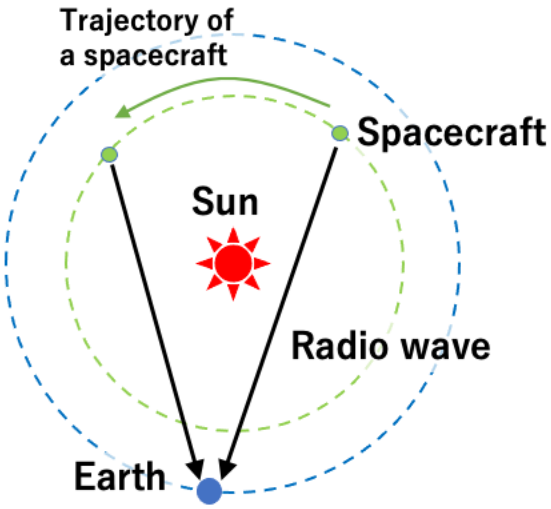

Figure 4. Schematic of the radio occultation observation of the solar corona using a spacecraft.

Various spacecraft have conducted radio occultation observations of the solar corona. Solar wind velocities were derived from intensity spectra similarly to IPS observations (Efimov 1994; Imamura et al. 2014). Efimov et al. (2010, 2012) detected quasi-periodic electron density fluctuations, which they call quasi-periodic component (QPC) and identified as acoustic waves, in the corona using radio occultation experiment with the Mars Express, Venus Express, and Rosetta. Mean periods of the QPCs studied by Efimov et al. (2010, 2012) were about 3–4 minutes. Since the cut-off period of acoustic waves drops to 150 s in the transition region below the corona (Erdélyi et al. 2007), acoustic waves with periods exceeding 150 s should not have propagated from the photosphere.

The Venus orbiter Akatsuki is a spacecraft launched by JAXA in 2011. Although Akatsuki usually observes the Venusian atmosphere with optical methods and radio occultation, radio occultation observations of the solar corona were conducted during the passage of the spacecraft on the opposite side of the sun as seen from the Earth (solar superior conjunction). Akatsuki has conducted radio occultation observation campaigns in 2011, 2016, 2018, and 2019, covering various solar activity phase from the maximum (year 2011) to the minimum (year 2019). Using Akatsuki's radio occultation data in 2011, Imamura et al. (2014) estimated solar wind velocities from the scintillation spectra and confirmed the solar wind acceleration in the region of 1.5–20.5 R_S. Using the same data set, Miyamoto et al. (2014) detected quasi-periodic density fluctuations that are considered to be acoustic waves and derived the radial dependences of the wave's amplitudes, periods, coherence times, density amplitudes, and energy fluxes. They also suggested that acoustic waves originating from Alfvén waves are breaking, and the wave energy is thermalized at heliocentric distances farther than ~6 R_S (Figure 5).

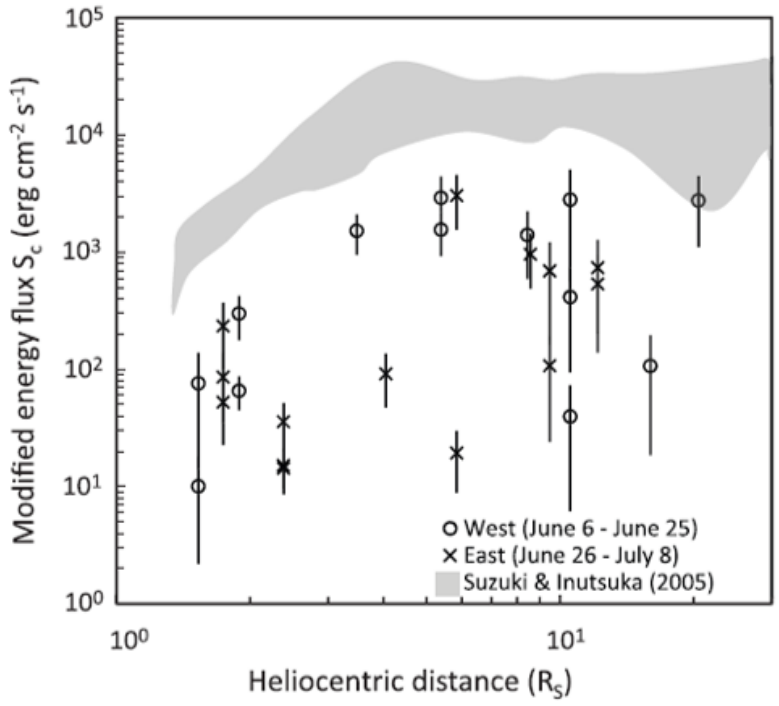

Figure 5. Radial distribution of the energy flux obtained from the observations on the western side (circles) and the eastern side (crosses) of the Sun. A result obtained from Akatsuki's radio occultation campaign in 2011 by Miyamoto et al. (2014). Shaded area represents the result of the numerical model by Suzuki and Inutsuka (2005).

1.3. Purpose of this study

As mentioned above, it was suggested that acoustic waves and turbulence can be generated in the corona and play important roles in coronal heating and solar wind acceleration. The difference of physical process between the fast wind and the slow wind will provide clues to the mechanism for the acceleration. In this study, by using spacecraft radio occultation, we aim to clarify what makes the difference between the fast and slow winds by deriving the radial distributions of the solar wind velocity, the turbulence characteristics, and the characteristics of acoustic waves in different types of the solar wind.

In this paper, we report the results of analyses of radio signals transmitted from JAXA's Venus orbiter Akatsuki and received at a ground station during the solar superior conjunction in 2016. First, in section 2, we introduce the details of the data set used in the analysis and describe how the time series of the intensity variation and the frequency/phase variations were derived from the recorded signals. The solar wind velocity map obtained by

IPS observations conducted by the Solar-Terrestrial Environment Laboratory (STEL) at Nagoya University is also introduced to locate the regions observed by Akatsuki in the horizontal velocity distribution. In section 3, we derive the solar wind velocity and the spatial structure of turbulence from the intensity variation. In section 4, acoustic waves are extracted from the frequency fluctuation and the amplitude, period, density amplitude, and energy flux of each of the detected waves are derived. The conclusions are given in section 5.

2. Observations

The observations of the solar corona were conducted from May 30 to June 15 in 2016 using the 8.4 GHz downlink signal of JAXA's Venus orbiter Akatsuki during solar conjunction. The total of 11 experiments covered heliocentric distances of 1.5–20.5 R_S (Figure 6).

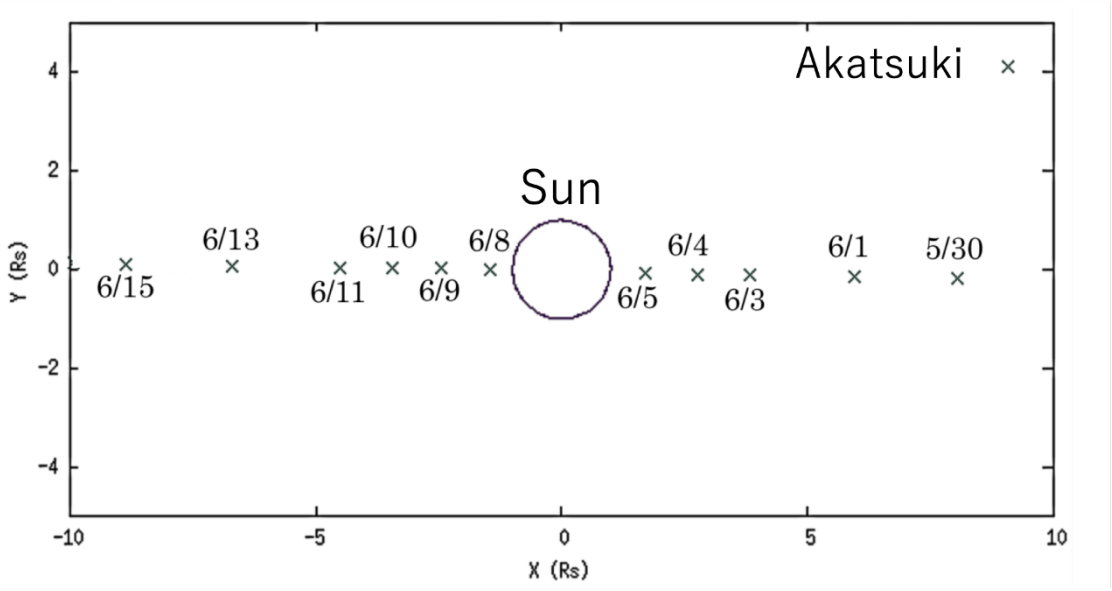

Figure 6. Location of Akatsuki (crosses) relative to the sun (circle) as seen from the Earth on the dates of the observations in 2016.

Table1 summarizes the observations. The former half period (May 30 to June 5) covers the western side of the sun, and the letter half (June 8 to 15) covers the eastern side of the sun. The recording was done for 5.5 hours in each of the 11 experiments. We limit our analysis to data taken at distances longer than 3.0 R_S since the data at closer distances suffer strong scattering and need different approaches (Imamura et al. 2014).

The measurements utilized the radio science subsystem of the Akatsuki spacecraft (Imamura et al. 2011, 2017). The experiments were conducted using the 8.4GHz downlink signal stabilized by an onboard ultra-stable oscillator (USO) having an Allan deviation of less than 10^{-12} at the integration time of 1–1000 s. The radio wave transmitted from the high-gain antenna of the spacecraft was received at Usuda Deep Space Center (USDC) of Japan for deep-space communication. The signal received was down-converted to ~2MHz

by an open-loop heterodyne system stabilized by a hydrogen master and 4-bits digitized with a sampling rate of 8MHz using a recorder developed for radio astronomy.

Table 1
Summaries of the observations.

2016 Date	Time (UT)	Length (hour)	Heliocentric distance (R_S)	East/West
May 30	02:00	5.5	8.19–7.95	West
June 1	02:00	5.5	6.08–5.83	West
June 3	02:00	5.5	3.94–3.69	West
June 4	02:00	5.5	2.87–2.62	West
June 5	02:00	5.5	1.80–1.56	West
June 8	02:00	5.5	1.36–1.60	East
June 9	02:00	5.5	2.36–2.56	East
June 10	02:00	5.5	3.33–3.58	East
June 11	02:00	5.5	4.41–4.66	East
June 13	02:00	5.5	6.59–6.84	East
June 15	02:00	5.5	8.75–9.00	East

Notes. "Time" is the start of recording signals, "Length" is the recording length in hours, "Heliocentric distance" is the heliocentric distance in the middle of each observation.

The time series of the intensity and the frequency were retrieved from the recorded data in the following manner (Imamura et al. 2005, 2011). First, the Doppler frequency time series predicted for the motions of the ground antenna and Akatsuki is subtracted from the recorded signal by heterodyning, thereby suppressing the frequency variation to enable narrow band-pass filtering. Then, the complex voltage data after subtracting the predicted Doppler frequency is divided into subsections with a certain width, and discrete Fourier transform (DFT) is applied to each section. A narrow spectral interval is extracted from each DFT spectrum, and an inverse Fourier transform is performed to realize a narrow band filtering. The absolute value of the complex data in the obtained narrow-banded signal represents the intensity of the received radio signal. Narrowing the bandwidth results in a larger signal-to-noise ratio at the expense of the time resolution. For the intensity time series, the time resolution was set to be 0.00256 s. The real and imaginary parts of each complex number in the obtained narrow-band signal also gives the phase from which the frequency can be obtained by time differentiation. However, the frequency time series

obtained by this procedure was found to be too noisy, and thus a different method is used. We further divided the narrow-banded signal into subsections and applied another DFT to each of the subsections, and a theoretical spectrum (sinc function) was fitted to the power spectrum to determine the frequency (Lipa and Tyler, 1979). The time resolution of the frequency time series is 1.3072 s.

The solar activity was in a decaying phase in 2016. The solar wind velocities at far distances were obtained by the interplanetary scintillation (IPS) observations conducted by the Solar-Terrestrial Environment Laboratory (STEL), Nagoya University during the same period. The measured velocities were projected onto the solar surface and the closest points along the radio ray path of Akatsuki are shown on the map in Figure 7. The radio occultation probed relatively high-speed regions near a coronal hole on June 1 and June 3 on the western side of the sun, while regions far from coronal holes were probed on other days.

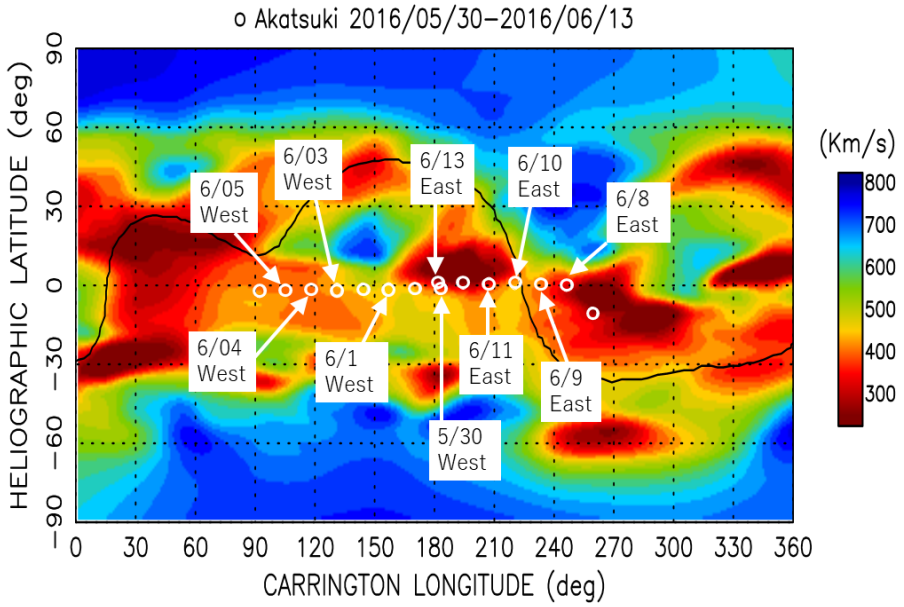

Figure 7. Solar wind velocity synoptic map generated with IPS measurements by the Solar-Terrestrial Environment Laboratory (STEL), Nagoya University (provided by Prof. Tokumaru). Circles pointed by arrows indicate the projections of the closest points along the ray path of Akatsuki radio occultation. The numerals indicate the dates of the observation, and "East" and "West" indicate the locations with respect to the sun as seen from the Earth. The blue region around the heliographic latitude of 15°N and the Carrington longitude of 150° corresponds to the fast solar wind originating from the coronal hole.

3. Intensity scintillation

From the intensity time series of the received radio signal, we can derive the flow speed and the turbulence characteristics following the procedure described below. The radio wave that traverses the solar corona is scattered, i.e., the wavefronts are disturbed, by density fluctuations, thereby producing a diffraction pattern at the Earth. The diffraction pattern at the Earth is convected past the observer at the solar wind velocity and is observed as intensity scintillations (Figure 8). Therefore, the intensity scintillation spectrum reflects the spatial structure of the coronal plasma and the solar wind velocity (e.g., Scott et al. 1983).

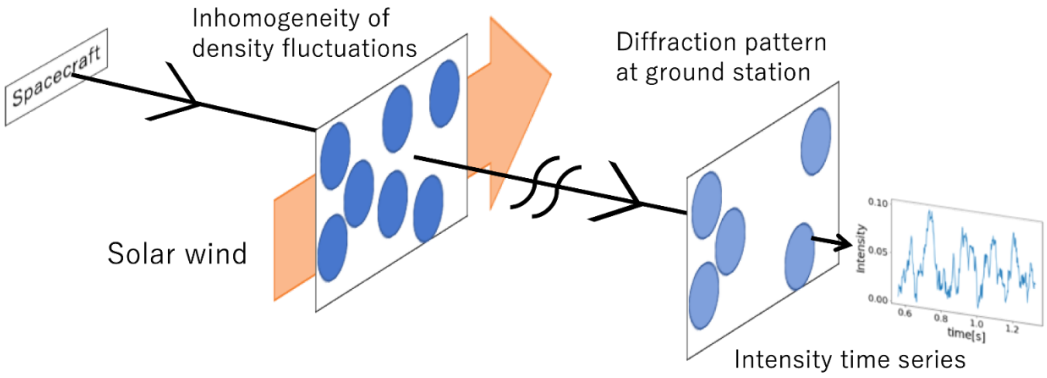

Figure 8. Schematic of the intensity scintillation observation.

The solar wind is thought to involve well-developed turbulence presumably generated by Alfven waves (e.g., Cranmer et al. 2007; Shoda et al. 2018). Then the spatial spectrum of the plasma density is expected to approximately follow the Kolmogorov power law in the inertial subrange. The turbulence dissipates at the inner scale where the kinetic energy is converted to heat. Because of the rapid increase in the plasma density with decreasing the distance to the Sun, the effect of the medium on the radio wave is represented by a thin phase modulator that is located at the point of closest approach to the Sun. Under these assumptions and the weak scattering approximation, the intensity scintillation spectrum is expressed as (Coles and Harmon 1978; Scott et al. 1983)

$$P(f) = \frac{2\pi(\lambda r_e)^2}{V}\int_{-\infty}^{\infty}\Phi_n\left(k_x = \frac{2\pi}{V}f, k_y\right)F_{diff}(k)dk_y \quad (1)$$

where V is the flow speed, f is the frequency of the received radio wave, λ is the wavelength of the received radio wave, r_e is classical electron radius, k_x is the wavenumber in the radial direction, k_y is the wavenumber in the direction perpendicular to the radial direction and the ray path, and

$$F_{diff} = 4\ \sin^2\left(k^2\frac{\lambda z}{4\pi}\right) \quad (2)$$

is the Fresnel propagation filter with $k = \sqrt{k_x^2 + k_y^2}$. The spatial spectrum of the plasma density is formulated as

$$\Phi_n = A\left(\sqrt{k_x^2 + \frac{k_y^2}{AR^2}}\right)^{-\alpha}\exp\left(-\frac{k^2}{k_c^2}\right)R^{-4} \quad (3)$$

where A is a constant, AR is the axial ratio of irregularities, α is the power law index of the turbulence spectrum, and k_c is the wavenumber
beyond which the turbulence begins to dissipate, which is related to the inner scale Si as $Si = 3/k_c$ (Scott et al. 1983). The Fresnel filter is a high-pass filter that suppresses frequency components lower than the Fresnel wavenumber $k_F = \pi/(\lambda z)^{1/2}$, with z being the distance from the Earth to the closest point. Because of this effect, the scintillation spectrum shows a knee around the Fresnel frequency defined by $f_F = V\,k_F/2\pi$. (Coles and Harmon 1978, Scott et al. 1983). The axial ratio AR indicates the ratio of the radial extension of the density inhomogeneity; $AR = 1$ when the inhomogeneity is isotropic. Though Scott et al. (1983) also considered the effect of the dispersion of the radial velocity V on the spectrum, the effect is similar to the one by the anisotropy, and thus we did not adopt the velocity dispersion as a fitting parameter here.

3.1. Spectral analysis

The power spectra of the intensity time series were obtained in the following manner. First, a polynomial function was fitted to each time series, and the fitted function was removed from the original to suppress low-frequency components. Then, the time series was divided

into 200 subintervals with lengths of ~100 seconds. FFT was applied to the subintervals, and the obtained power spectra were averaged to smooth out noisy structures. Since a noise floor appears at frequencies higher than ~100 Hz (Figure 9(a)), the noise level was estimated by calculating the mean power in the noise floor, and the estimated noise level was subtracted from the spectrum so that the structure at the inner scale is seen more clearly (Figure 9(b)). Resampling to have the same intervals in log scale and smoothing were also conducted after subtracting the noise floor.

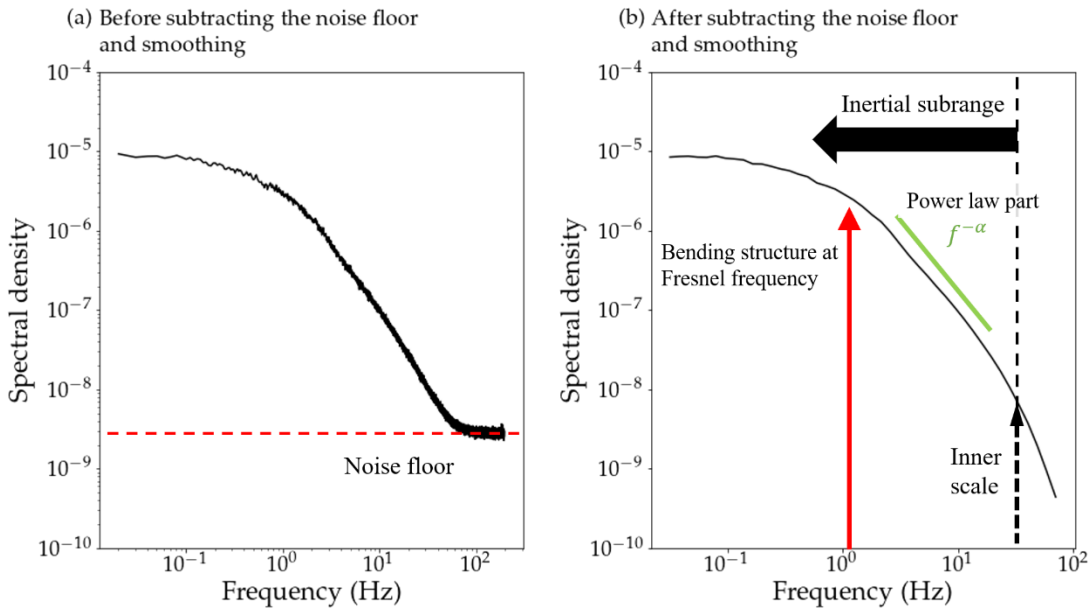

Figure 9. An example of the power spectra (a) before and (b) after subtracting the noise floor and smoothing. The data was obtained on June 1, 2016. The heliocentric distance at the tangential point was 6.1 R_S. In Fig. 9(a), the dashed red line shows the mean power of the noise floor, and the noise floor appear at higher frequency than ~100 Hz. In Fig. 9(b), the solid green line shows power law part indicative of the inertial subrange, the red arrow points to the Fresnel frequency, and the dashed black arrow points to the inner scale.

Figure 9(b) shows an example of the obtained intensity scintillation spectra after subtracting the noise floor and smoothing. The spectrum clearly exhibits characteristic structures. The solid red arrow points to the Fresnel knee, the solid green line shows a power-law part with an exponent of $-\alpha$ indicative of the inertial subrange, and the black dashed arrow points to the inner scale beyond which the dissipation of turbulence occurs.

Figure 10 shows all of the obtained intensity scintillation spectra. Each spectrum exhibits a

flattened part on the low frequency side, the Fresnel knee around 0.2–2 Hz, a power-law part indicative of the inertial subrange, and a steepening near the high-frequency end indicative of dissipation at the inner scale.

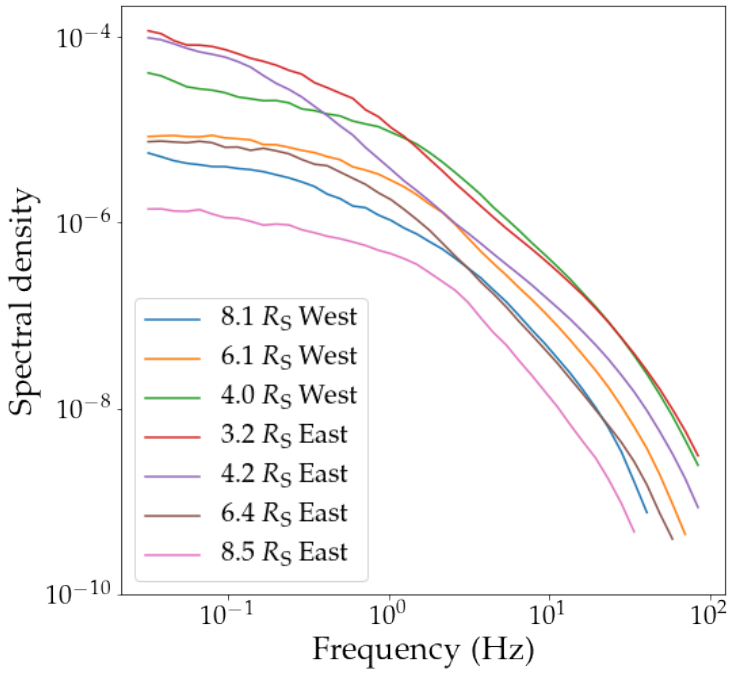

Figure 10. Observed intensity scintillation spectra. Numerals are the heliocentric distance in the unit of R_S.

By fitting the theoretical model spectrum (1) to the observed spectra, we can derive the unknown parameters included in the model. Such a model fitting has been applied to spectra of interplanetary scintillation (IPS) of natural radio sources (e.g., Woo and Armstrong 1981; Scott et al. 1983; Tokumaru et al. 1991). In this study, we retrieve the following five parameters from each spectrum: the solar wind velocity V, the power law index α, the axial ratio AR, the wavenumber corresponding to the inner scale k_c, and the magnitude of the power A. The procedure of the fitting is as follows.

First, to treat all parameters equally, we rewrite the model function so that each parameter is normalized by its initial value in the model function. The initial values are chosen so that the theoretical spectrum roughly matches the observed spectrum. The fitting is performed using the Python routine scipy.optimize.basinhopping; in this routine, a local optimal solution is found based on the initial values by using Limited-memory Broyden–Fletcher–

Goldfarb–Shanno (L-BFGS) method, which is one of the nonlinear optimization methods, and then a perturbation is added to the obtained optimal solution to adopt it as the new initial values. Repeating this process, we obtain the global optimal solution that does not fall into certain minima. The errors in the obtained parameters are estimated from the diagonal components of the error covariance matrix, which is calculated from the first order differential coefficient matrix near the fitting solution.

Figures 11–17 shows the results of the fitting, with the determined parameter values being indicated in each panel. We can see that the observed spectra are successfully fitted by the theoretical curve. The characteristic features such as the Fresnel knee, the power-law part and the steepening at the high-frequency end are reproduced in the fitted curves.

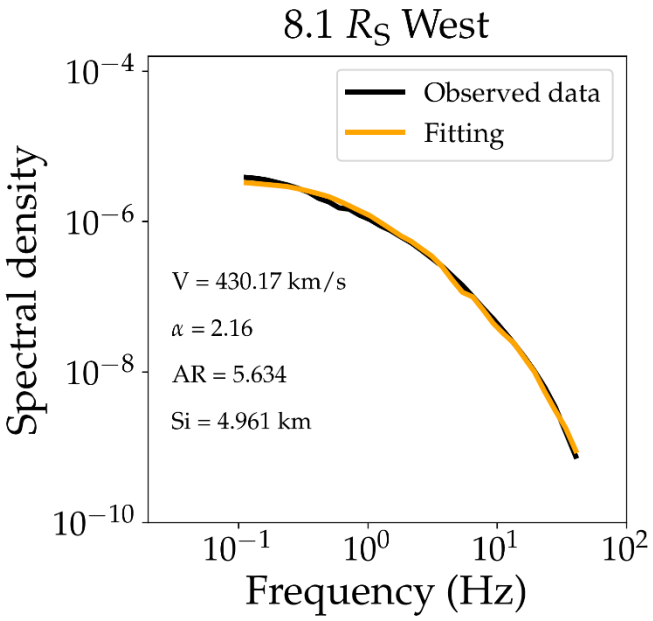

Figure 11. Scintillation spectrum obtained from the observation on May 30 (black) and the model fit (orange). The obtained parameter values are also given in the panel.

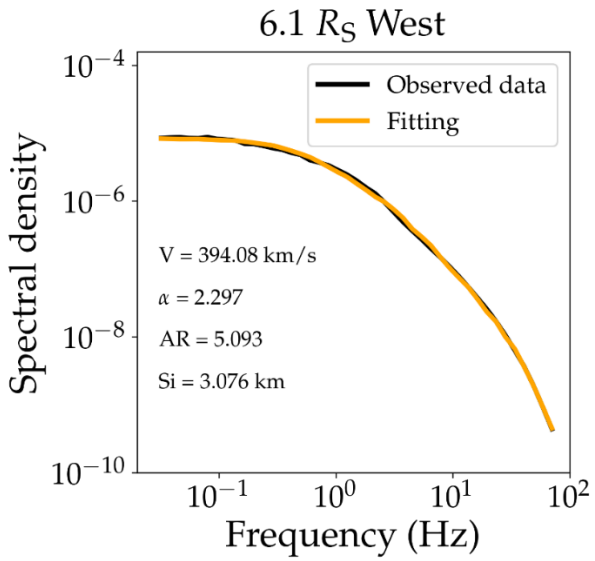

Figure 12. Scintillation spectrum obtained from the observation on June 1 (black) and the model fit (orange). The obtained parameter values are also given in the panel.

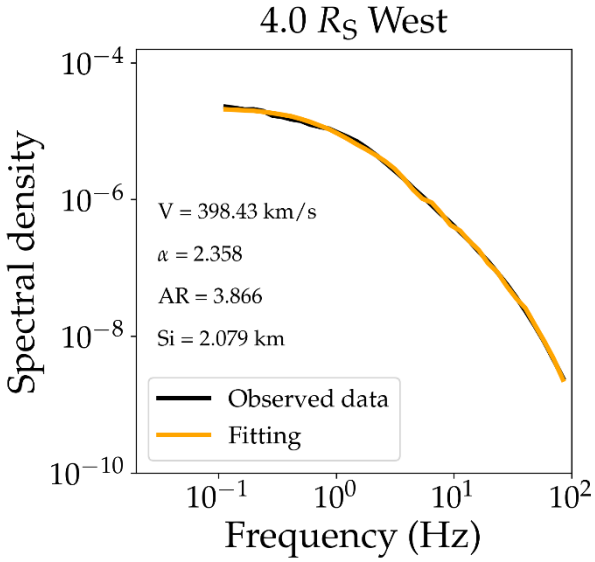

Figure 13. Scintillation spectrum obtained from the observation on June 3 (black) and the model fit (orange). The obtained parameter values are also given in the panel.

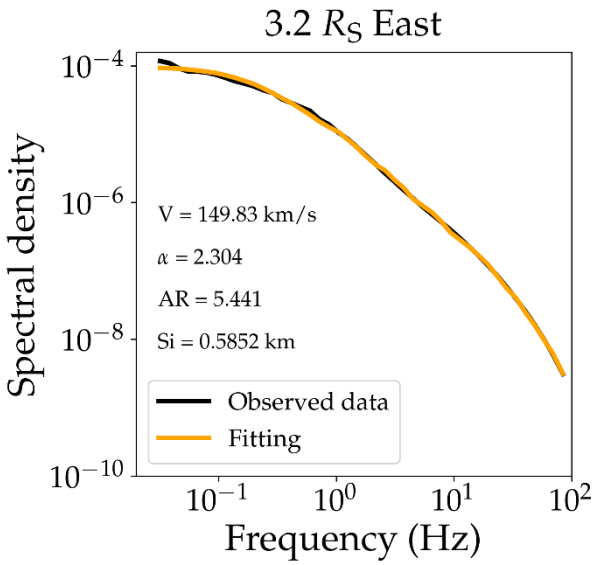

Figure 14. Scintillation spectrum obtained from the observation on June 10 (black) and the model fit (orange). The obtained parameter values are also given in the panel.

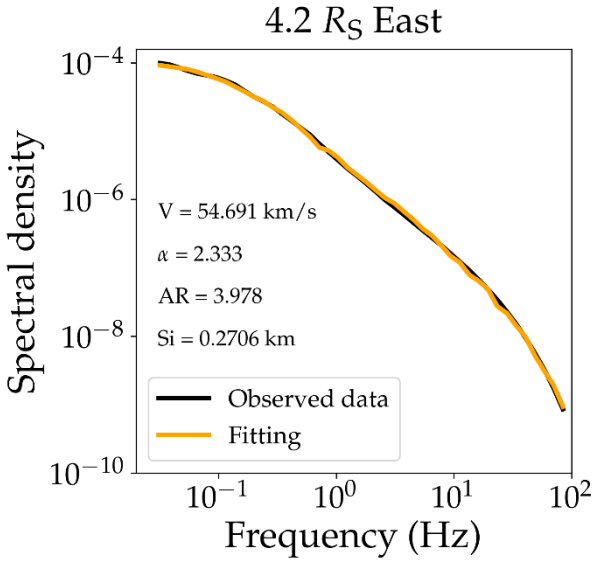

Figure 15. Scintillation spectrum obtained from the observation on June 11 (black) and the model fit (orange). The obtained parameter values are also given in the panel.

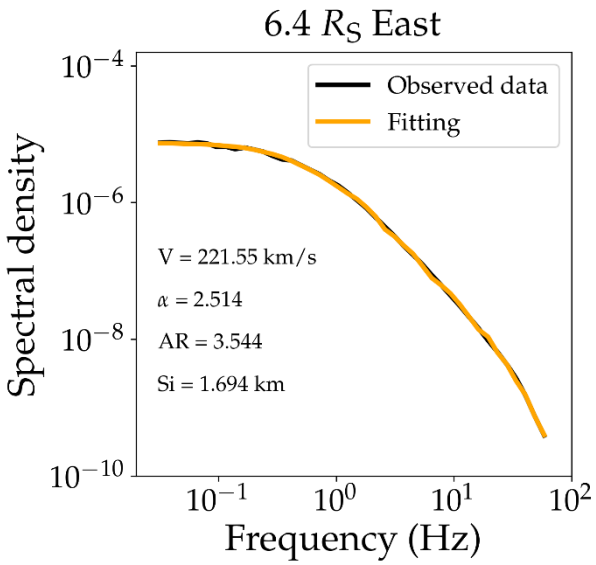

Figure 16. Scintillation spectrum obtained from the observation on June 13 (black) and the model fit (orange). The obtained parameter values are also given in the panel.

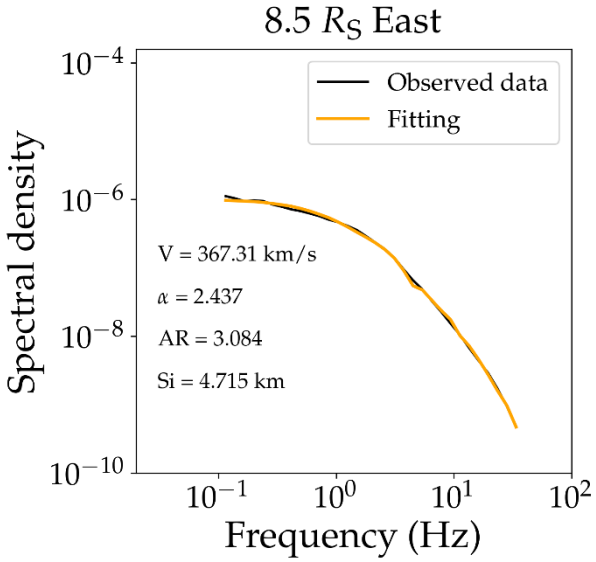

Figure 17. Scintillation spectrum obtained from the observation on June 15 (black) and the model fit (orange). The obtained parameter values are also given in the panel.

3.2. Radial distributions of physical quantities

Figure 18 shows the radial distributions of the parameters obtained by parameter fitting. Filled circles show observations on the western side and crosses show observations on the eastern side. The observations near the coronal hole (Fig. 7) are also indicated. The solar wind velocity (Fig. 18(a)) increases with distance on the eastern side where the influence of the coronal hole is absent. The shaded area indicates the solar wind velocity obtained by Akatsuki's radio occultation observations in 2011 (Imamura et al. 2014). In 2011 observations, they measured the solar wind originating from closed loops in quiet-Sun. From the comparison of the observations in 2011 and 2016, we can see that the velocities in 2016 are faster than those in 2011 even if both of them probed regions above closed loops. The velocities near the coronal hole indicated by red circles on the western side are faster than those on the eastern side at similar distances. This suggests that these observations detected streams from the coronal hole. The power-law exponents (Fig. 18(b)) are generally smaller than the Kolmogorov law's value of $-11/3$, implying that the turbulence of the solar wind is not ideal turbulence. The axial ratio (Fig. 18(c)) is generally large, but a particular trend is hardly seen due to the large error. The inner scale (Fig. 18(d)) increases with distance and shows larger values in the streams that are thought to be originated from the coronal hole than in the other regions.

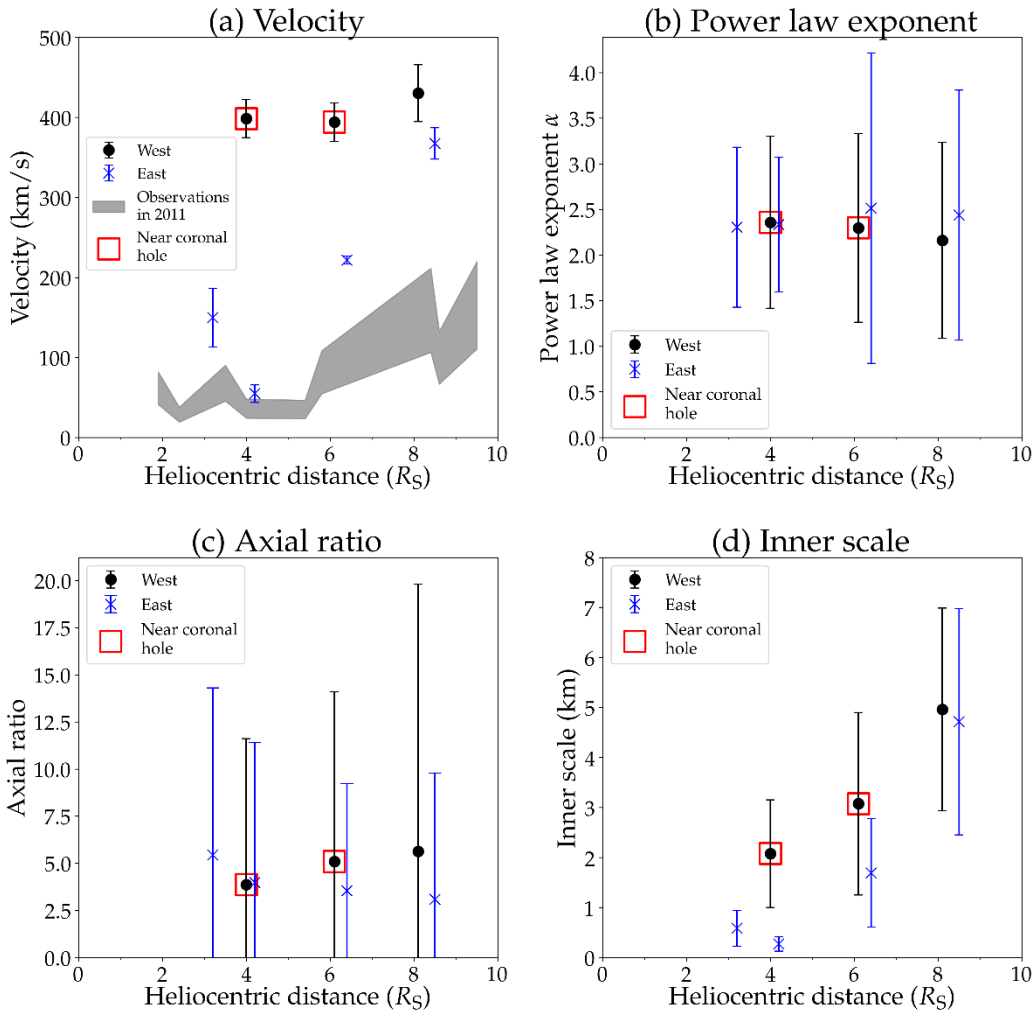

Figure 18. Radial distributions of the estimated parameters: (a) solar wind velocity, (b) power law exponent, (c) axial ratio, and (d) inner scale. Filled circles and crosses indicate observations on the western and eastern sides, respectively. Red open squares indicate the observations near the coronal hole on June 1 and June 3. The shaded area in Fig. 18(a) indicates the solar wind velocities in closed-loop regions obtained by Akatsuki's radio occultation observations in 2011 (Imamura et al. 2014).

3.3. Comparison of theoretical models of the dissipation scale

When energy is injected into turbulence at a large scale, it is transferred to smaller scales through the nonlinearity of the fluid. At a particular small scale, the plasma can no longer maintain its properties as a fluid, and the kinetic energy of plasma is converted to heat. This

transition scale where particle motions become important and turbulence dissipates is called "inner scale". There are models about the inner scale in the solar wind.

Here we compare the observations with two theoretical models: the inertial length model and the proton gyroradius model. The proton inertial length model relates the inner scale to the cyclotron damping of electromagnetic waves due to fluid motions at the Alfvén velocity. This model expresses the inner scale by using the plasma density of the corona (Coles and Harmon 1989; Yamauchi et al. 1998):

$$s_i = 3\frac{V_A}{\omega_c} = 684\frac{1}{\sqrt{N_e}} \text{ km} \quad (4)$$

where V_A is the Alfvén velocity and ω_c is the proton cyclotron frequency, N_e is the plasma density in unit of cm^{-3}. According to this model, the inner scale is larger for lower densities. On the other hand, the proton gyroradius model relates the inner scale to the gyroradius of the proton moving at the thermal velocity. Then the inner scale is given by

$$s_i = \frac{\mu v_{th}}{eB} = \frac{102\sqrt{\mu T_i}}{B} \text{ cm} \quad (5)$$

where μ is the ratio of the mass of an ion to mass of a proton (taken to be 1 in this situation), e is the elementary charge, T_i is the proton temperature in eV, and B is the magnetic field in G. According to this model, the higher temperature of the solar wind or the weaker background magnetic field, the larger the inner scale.

In our results, the inner scale generally increases with distance. Similar trends have been reported by Coles and Harmon (1989), Yamauchi et al. (1998) and Raja et al. (2019). Such a tendency is qualitatively consistent with both of the inertial length model and the proton gyroradius model since N_e and B decrease with distance.

The observations near the coronal hole exhibit lager inner scales than other observations at similar distances. Yamauchi et al. (1998) showed, based on IPS observations, that the inner scale is similar between the slow wind and the fast wind at distances of >20 R_S; the difference at closer distances has not been observed. Considering that the fast wind originating from the coronal hole is thought to have lower densities and stronger magnetic fields than other regions (Altschuler et al.1972), our results are qualitatively consistent with the proton inertial length model and conflict with the gyroradius model.

Figure 19 compares the observed inner scales and the theoretical models (4) and (5). The plasma density used in the computation is represented by the empirical model proposed by

Pätzold et al. (1987):

$$N_e = \left(\frac{5.79}{R^{16}} + \frac{1.6}{R^6} + \frac{9.2 \times 10^{-3}}{R^2}\right) \times 10^8 \text{ cm}^{-3} \quad (6)$$

The ion temperature is set to 10^6 K and the magnetic field is represented by Dulk and McLean's (1978) empirical model for the distances of 1.02–10 R_S:

$$B(R) = 0.5\ (R-1)^{-1.5} \text{ G} \quad (7)$$

As we can see in Fig. 19, the estimated inner scales are closer to the inertial length model than the proton gyroradius model, about one order of magnitude larger than the proton gyroradius model. Raja et al. (2019) argued, based on interferometric observations using natural radio sources, that observed inner scales are consistent with the proton gyroradius model. In contrast to our estimates of several kilometers around 2–8 R_S, the values derived by Raja et al. (2019) are less than 1 km at 10–20 R_S with an exceptionally large value of 13.5 km at 2.2 R_S. It is quite different from our results, but the reason is not unclear.

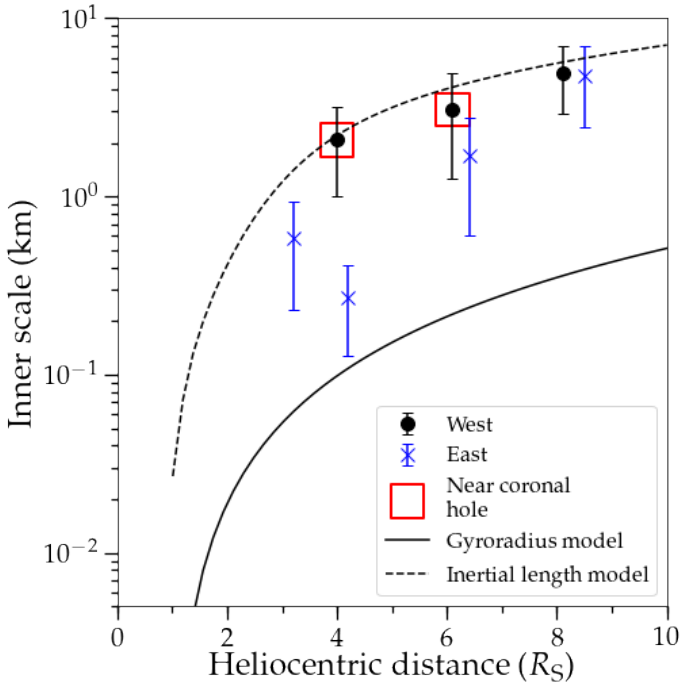

Figure 19. Comparison between the observed inner scales and theoretical models. The plots of the observed data are the same as in Figure 18. The dashed line represents the inertial length model, and the solid line represents the gyroradius model.

4. Phase/frequency fluctuation

4.1. Phase fluctuation spectra

The phase fluctuation of the received radio wave represents the density fluctuation along the ray path caused by turbulence and waves in the solar wind (Figure 20). The phase shift $\delta\phi$ due to the density fluctuation is related to the column density fluctuation δN_e as

$$\delta\phi = \frac{\alpha}{c}\,\delta N_e \tag{8}$$

where c is the speed of light, $\alpha = e^2/8\pi^2\varepsilon_0 m_e$ ~40.3 $m^3 s^{-2}$ with ε_0 being the dielectric constant of the vacuum, and m_e being the electron mass. Because of this relationship and the turbulent nature of the density inhomogeneity, the power spectrum of the phase fluctuation exhibits a power law part representing turbulence and the inflection at the inner scale (e.g., Woo and Armstrong 1979; Coles et al. 1991; Pätzold et al. 1996; Imamura et al. 2005).

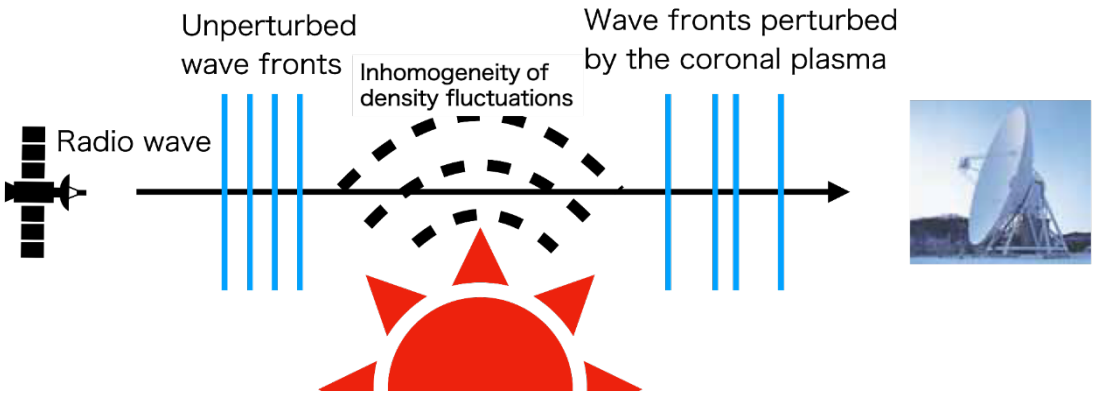

Figure 20. An illustration of the phase scintillation observation.

In this section, we derived power spectra of phase fluctuations of the radio waves and compared the shape of the power spectrum with distance by the same procedure of the derivation of the intensity power spectrum.

Figure 21 shows the power spectra of the phase fluctuation for all observations. Each spectrum is the average of the spectra of ~2000 s subintervals in the whole time series. The

noise floor was estimated from the level near the high-frequency end and subtracted from the spectrum similarly to the scintillation spectra. Fig. 21a and Fig. 21b are for the observations on the western side and the eastern side, respectively. On both sides, each spectrum follows a single power law in the frequency range 0.1–10 Hz at distances closer than ~4 R_s, suggesting that turbulence dominates in the density fluctuation. On the other hand, at distances beyond ~6 R_s, the power law exponent changes around 0.5–2 Hz (arrows in Fig. 21). This can be interpreted as the presence of an excess power in addition to turbulence on the low-frequency side. Acoustic waves, that are observed as quasi-periodic components (QPCs) (Efimov et al. 2010, 2012; Miyamoto et al. 2014), might be responsible for the excess power. We will investigate the characteristics of such wave disturbances using the same data set in the next section.

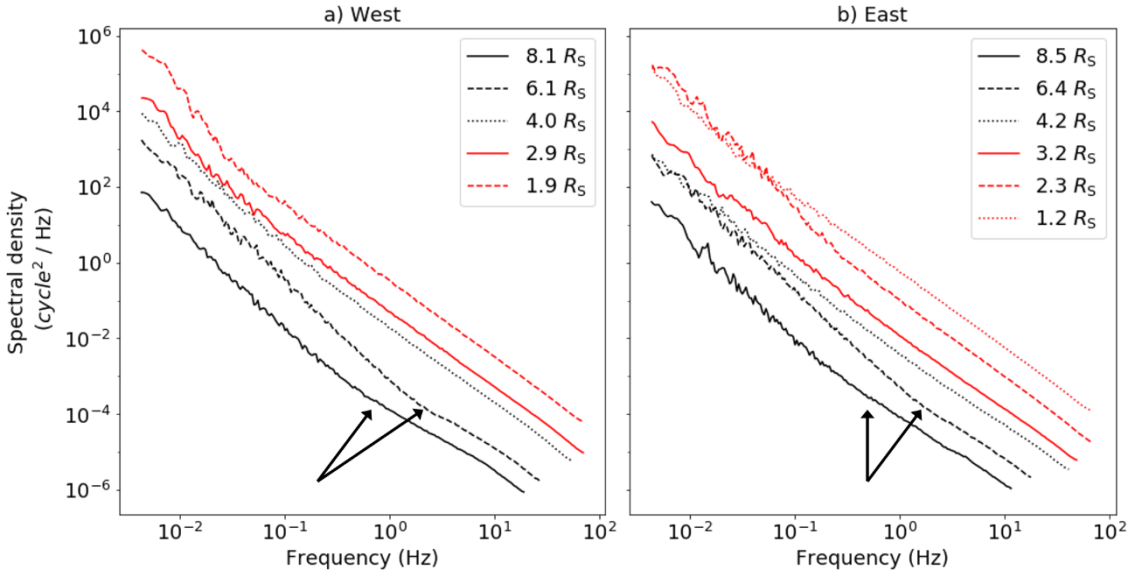

Figure 21. Observed phase scintillation spectra on a) the western side and b) the eastern side. Beyond ~6 R_S, the power spectrum cannot be represented by a single power law. Arrows point to the inflections where the power law exponent changes.

4.2. Quasi-periodic density fluctuations

As Efimov et al. (2010, 2012) and Miyamoto et al. (2014) demonstrated, quasi-periodic density fluctuations that traverse the ray path can be observed as the variations in the

frequency/phase of the received signal. Such quasi-periodic fluctuations are interpreted as acoustic waves. To study the characteristic of localized wave packets, we applied wavelet analysis to the frequency time series and quantified the amplitude, the period, and the coherence time of each wave event. The density amplitude and the energy flux are also estimated following the method of Miyamoto et al. (2014).

First, we remove low-frequency components by fitting a third-order polynomial to each frequency time series and subtracting it from the original. Then wavelet power spectra were obtained by using the wavelet transform routine in the Python-based PyCWT ecosystem, which is based on Torrence and Compo (1998). The Morlet function was used as the wavelet basis function. Figure 22 shows the shape of the Morlet function (Torrence and Compo 1998), and its shape represents a wave packet. We used the frequency time series data normalized by standard deviation for wavelet analysis.

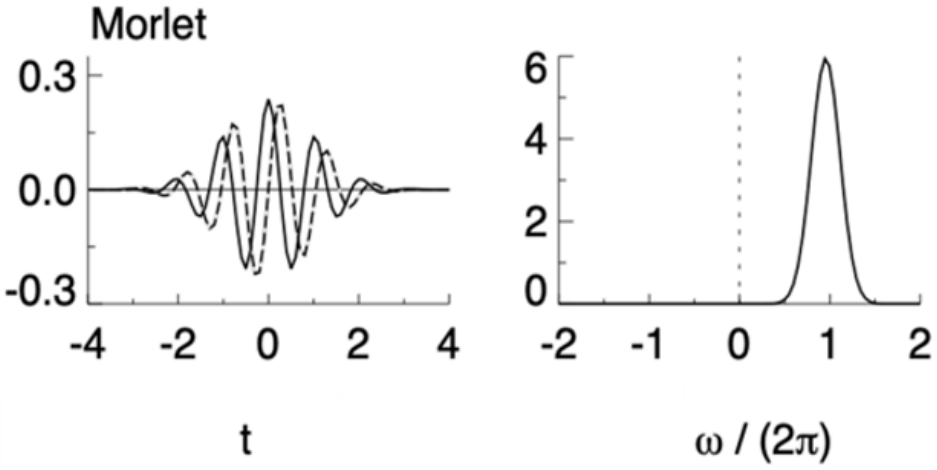

Figure 22. Shape of the Morlet function. The plot on the left gives the real part (solid) and the imaginary part (dashed) in the time domain, where t is the time and s is the wavelet scale. The plot on the right gives the wavelet in the frequency domain, where ω is the frequency (Torrence and Compo 1998).

Figures 23–33 show the frequency time series after subtracting the low-frequency components and the obtained wavelet power spectrum for each observation. We detected spectral peaks enclosed by the 95% confidence level, which is indicated by black lines, and identified them as wave packets. Approximately half of the wave packets fell outside the cone of influence (COI), which is the region where the effect of the discontinuity at the

edge of the time series becomes significant, were used in the later analyses. The length of each wave event, i.e., the coherence time (Miyamoto et al. 2014), was taken to be the duration in which the power continues to exceed the 95% confidence level. The frequency of the peak power is regarded as the frequency of the wave. Furthermore, we excluded wave packets which have shorter coherence times than their respective periods since they can result from noise.

We detected about ten wave packets in each observation regardless of the heliocentric distance. Most of the wave packets have periods ranging 1–1000 s. The typical periods of the QPCs measured by the radio occultation observations by Ulysses, Galileo, Mars Express, Venus Express, and Rosetta spacecraft were about >170 s at distances of 3–10 R_S, and periods of the wave packets detected by Miyamoto et al. (2014) were 100–2000 s. Our results are similar to these previous results.

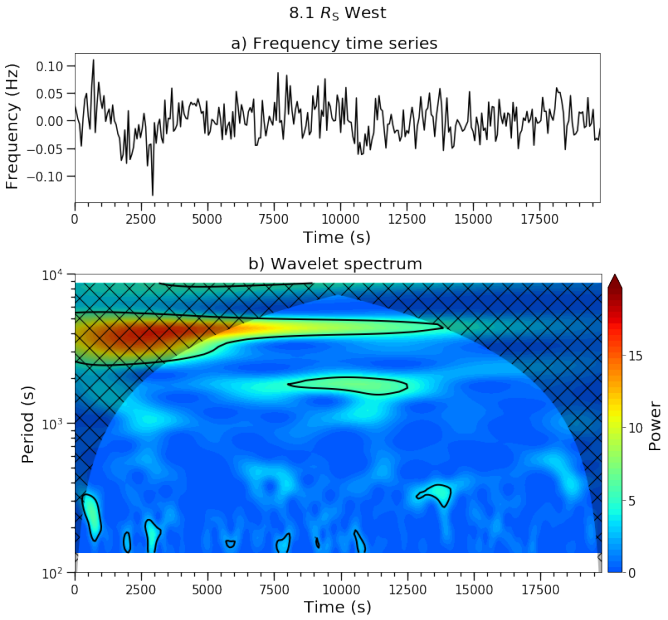

Figure 23. (a) Time series of the frequency fluctuation and (b) the wavelet power spectrum. The data was obtained on May 30, 2016. The heliocentric distance at the tangential point was 8.1 R_S. The wavelet power is normalized by the variance of the time series. The shaded region is the cone of influence (COI), which is the region where the effect of the discontinuity at the edge of the time series becomes significant. The black lines indicate the 95% confidence level.

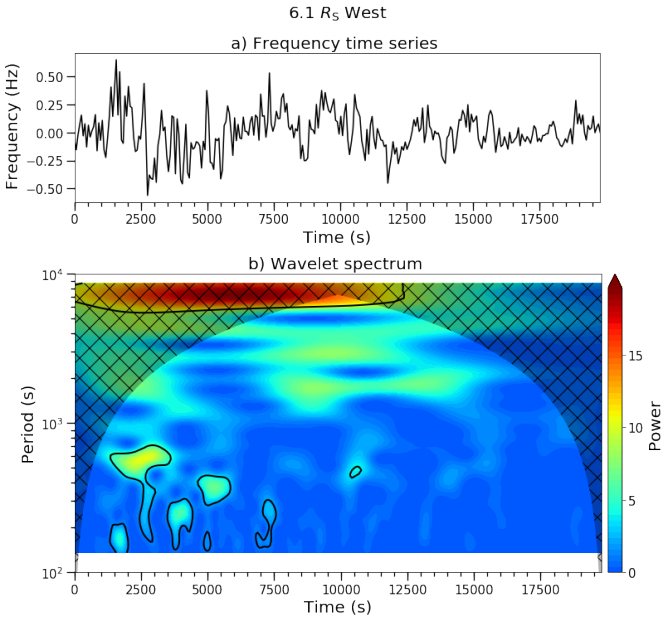

Figure 24. Same as Fig. 23, but for the data was obtained on June 1, 2016. The heliocentric distance at the tangential point was 6.1 R_S.

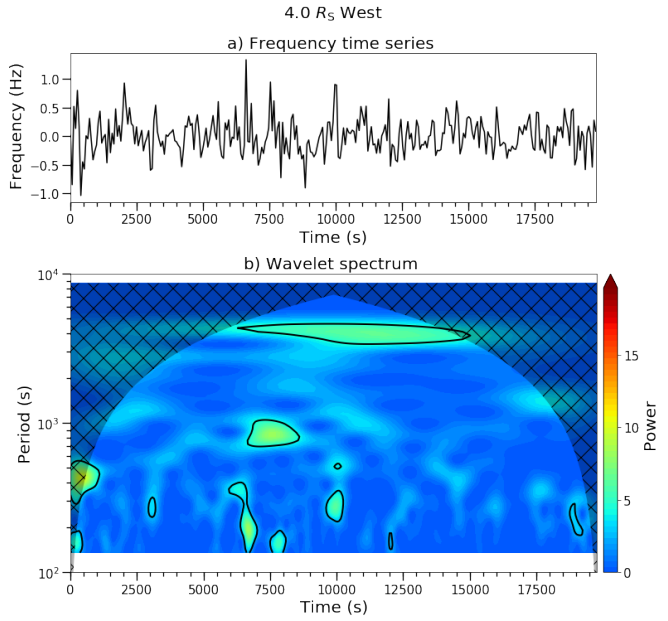

Figure 25. Same as Fig. 23, but for the data was obtained on June 3, 2016. The heliocentric distance at the tangential point was 4.0 R_S.

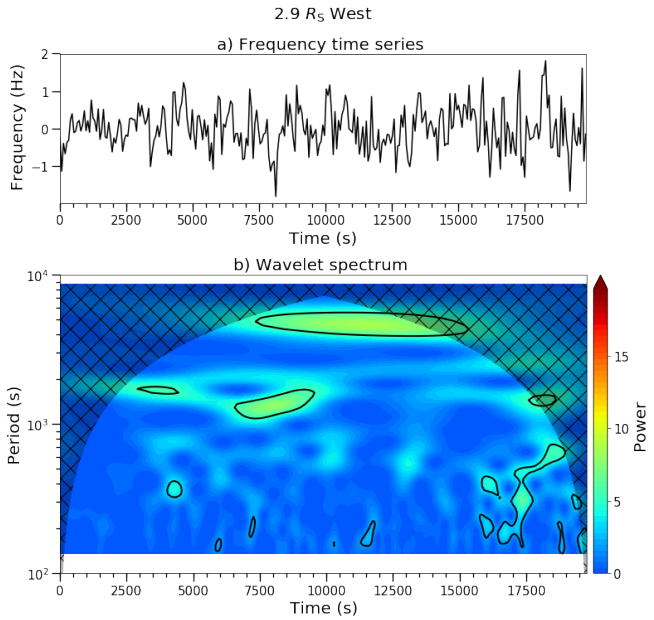

Figure 26. Same as Fig. 23, but for the data was obtained on June 4, 2016. The heliocentric distance at the tangential point was 2.9 R_S.

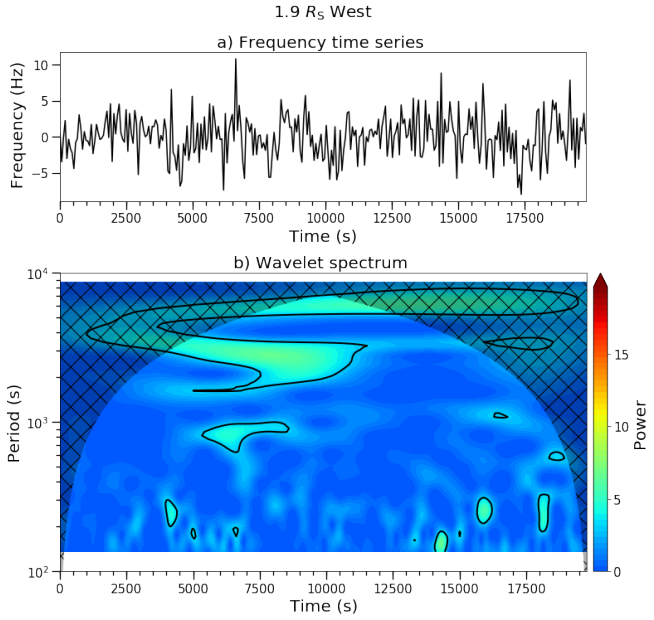

Figure 27. Same as Fig. 23, but for the data was obtained on June 5, 2016. The heliocentric distance at the tangential point was 1.9 R_S.

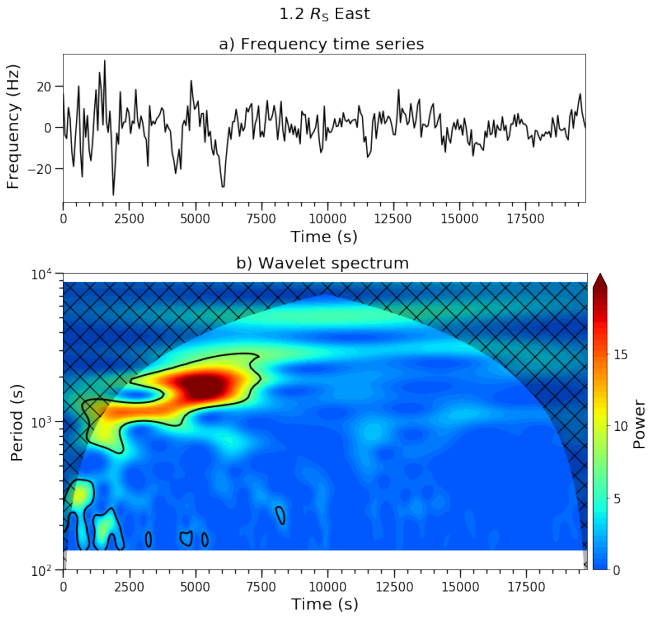

Figure 28. Same as Fig. 23, but for the data was obtained on June 8, 2016. The heliocentric distance at the tangential point was 1.2 R_S.

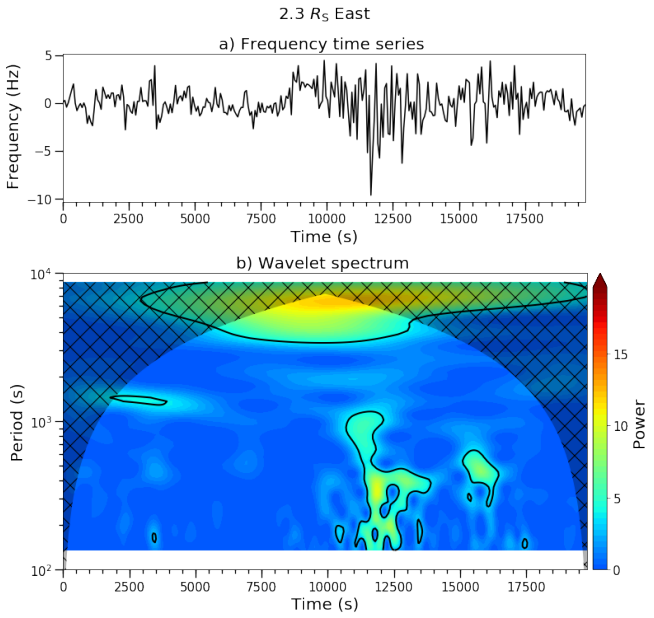

Figure 29. Same as Fig. 23, but for the data was obtained on June 9, 2016. The heliocentric distance at the tangential point was 2.3 R_S.

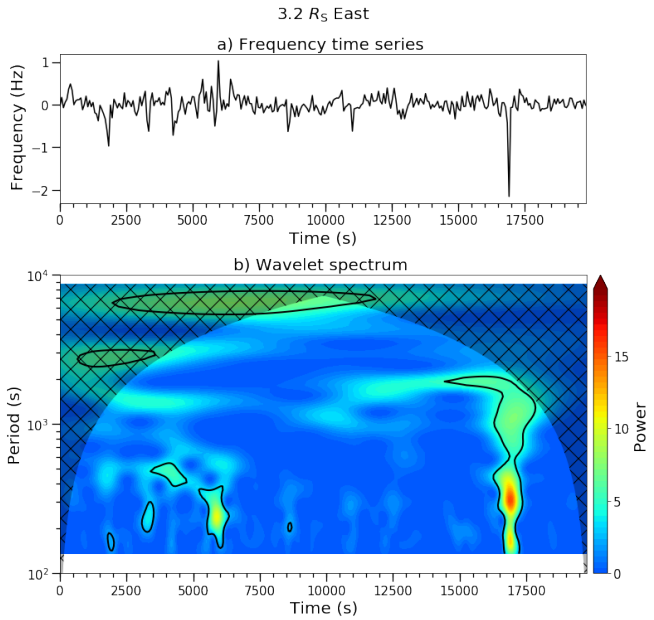

Figure 30. Same as Fig. 23, but for the data was obtained on June 10, 2016. The heliocentric distance at the tangential point was 3.2 R_S.

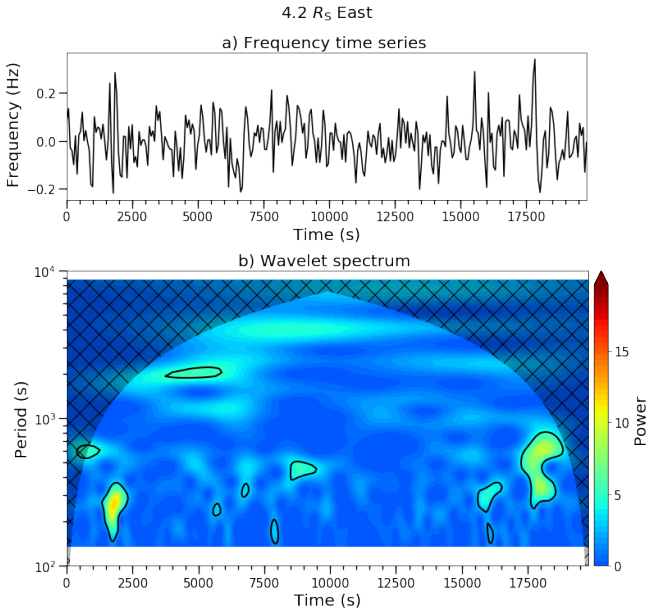

Figure 31. Same as Fig. 23, but for the data was obtained on June 11, 2016. The heliocentric distance at the tangential point was 4.2 R_S.

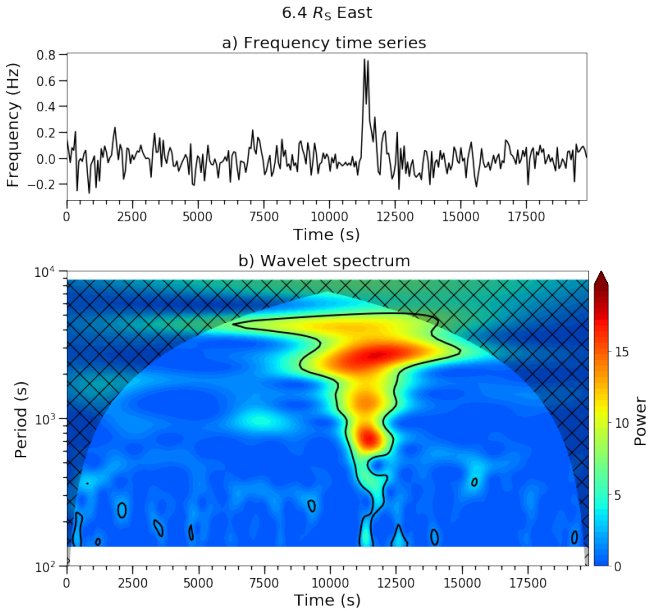

Figure 32. Same as Fig. 23, but for the data was obtained on June 13, 2016. The heliocentric distance at the tangential point was 6.4 R_S.

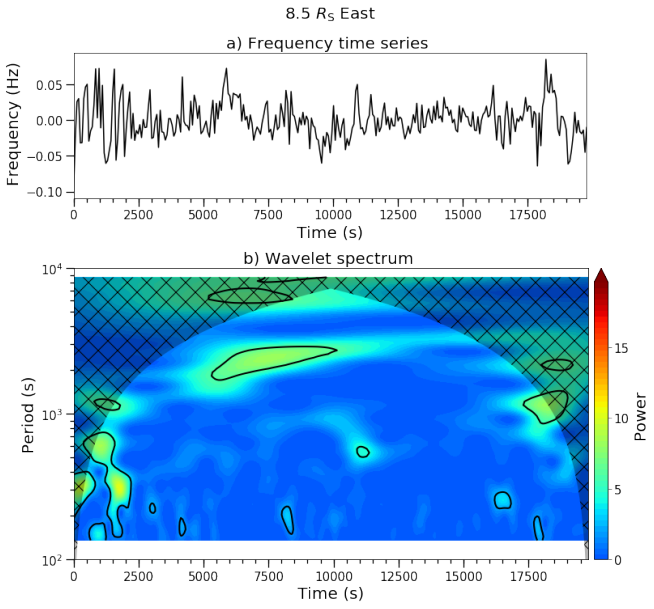

Figure 33. Same as Fig. 23, but for the data was obtained on June 15, 2016. The heliocentric distance at the tangential point was 8.5 R_S.

4.3. Density fluctuation and acoustic wave energy flux

We estimated the frequency amplitude of each detected wave packet f' from the peak value of the spectral density P and the full-width at half maximum B in the frequency following the method of Miyamoto et al. (2014):

$$f' = \sqrt{2PB} \tag{9}$$

The frequency perturbation δf is related to the fluctuation of the electron column density integrated along the path of the radio wave, *N*, as (Imamura et al. 2010)

$$\delta f = \frac{\alpha}{cf}\frac{dN}{dt} \tag{10}$$

where t is the time. Suppose that N oscillates at a period T, the relationship between the amplitude of the frequency fluctuation f' and that of N, N', is given by (Miyamoto et al. 2014)

$$f' = \frac{2\pi\alpha}{cfT}N' \tag{11}$$

Using this relationship, we can estimate N' from the observed f'. It should be noted that N' is an integral quantity along the ray path and that the density fluctuation associated with the wave packet occupies a small fraction along the ray path. The quantity that is directly related to the wave characteristics is not N' but the local density amplitude n'. Following Miyamoto et al. (2014), we assume the size of the density fluctuation along the ray path is the same as the length of the wave packet in the radial direction, which given by $T_{coh}(v_s + V)$, where T_{coh} is the coherence time of the wave event, v_s is the sound speed. Then n' is obtained as

$$n' = \frac{N'}{T_{coh}(v_s + V)} \tag{12}$$

Here, assuming the temperature of $T_i \sim 10^6$ K, the sound speed is calculated as $v_s = \sqrt{\gamma k_B T_i/\mu}$ km/s ~160 km/s with γ being the aideabatic index, and k_B being the Boltzman constant. V and T_{coh} are taken from our analysis.

The left panel of Figure 34 shows the column density amplitudes of the detected wave packets along the heliocentric distance, and the right panel shows the electron density amplitudes. Both amplitudes decrease with distance. At each distance, waves with longer periods tend to have larger amplitudes; this tendency is more pronounced in the column density than in the local density.

Both amplitudes in the fast solar wind originating from the coronal hole around 4 R_S and 6 R_S also tend to surpass those from other regions at similar distances, although the difference at ~6 R_S is not large.

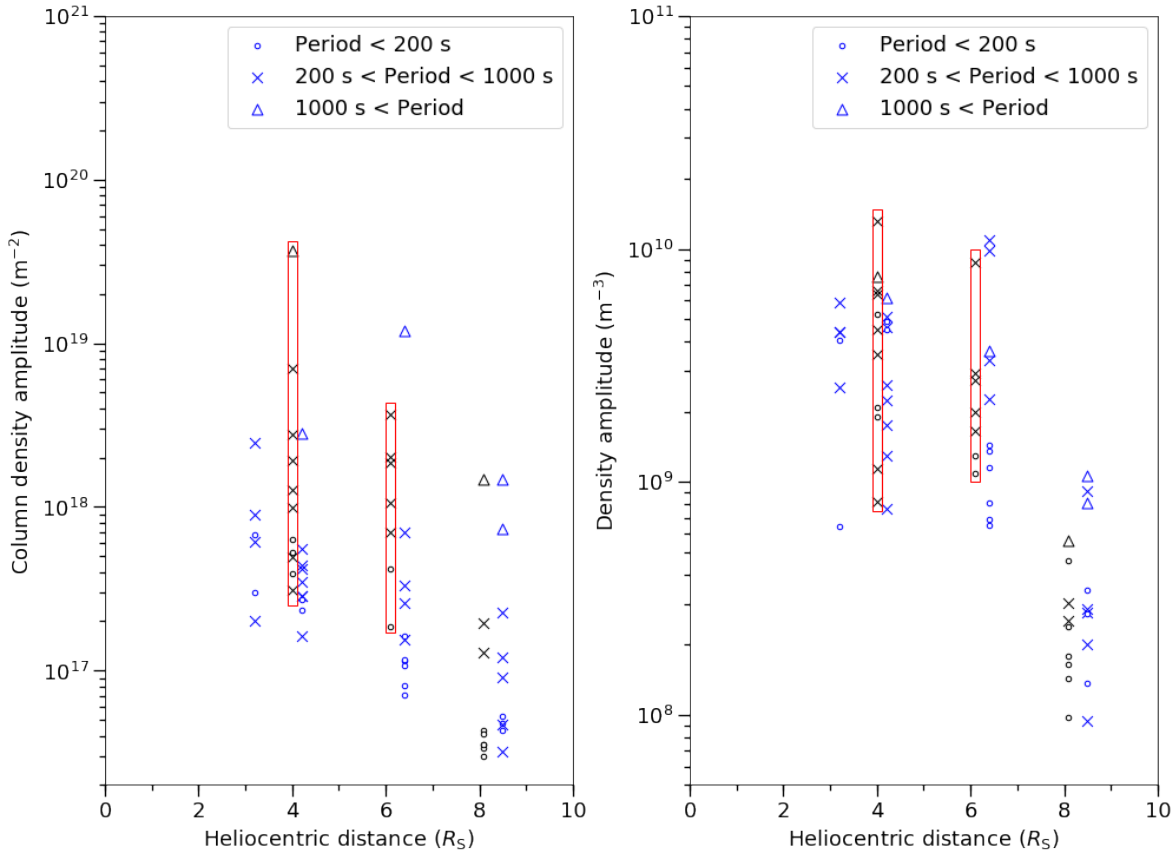

Figure 34. Radial distributions of (left) the electron column density amplitude and (right) the electron density amplitude of the detected wave packets. Black symbols show observations on the western side of the sun and blue symbols show observations on the eastern side. Filled circles indicate periods shorter than 200 s, crosses indicate periods of 200–1000 s, and triangles indicate periods longer than 1000 s. The red squared regions represent the observations which measured the fast solar wind originating from the coronal hole.

Next, we derive the amplitude of the fractional density fluctuation n'/n_0 as an indication of the nonlinearity of compressive waves. When n'/n_0 is close to 1, nonlinearity becomes important and the wave can break through the generation of a shock wave. We adopt the empirical model (6) proposed by Pätzold et al. (1987) for the radial variation of the background electron density n_0. This model is for solar maximum, and thus it is relevant to the slow wind.

Figure 35 shows the radial distribution of the fractional density amplitude. The amplitude generally increases with distance, becomes maximal around ~6 R_S, and decays beyond 6 R_S. The tendency to take the maximum around 6 R_S appeared also in Akatsuki's radio occultation in 2011 (Miyamoto et al. 2014). We can also see fractional density fluctuations are more than 10% around ~6 R_S. If we take the typical amplitude of 10% as it is, it is unlikely that acoustic waves break and generate shock waves. However, considering that there are wave packets with fractional density amplitudes of more than 40–50% around ~6 R_S and that the procedure of the derivation include various assumptions, it is reasonable that a fraction of waves reaches large amplitudes leading to shock formation and breaking around ~6 R_S.

The fractional density amplitudes in the fast solar wind originating from the coronal hole around 4 R_S tend to surpass those from other regions at similar distances, though the difference is not large. We should note, however, that we have used the same background density model both for the fast wind and the slow wind. Considering that the fast wind can have densities an order of magnitude lower than the slow wind (Altschuler et al.1972; Yamauchi et al. 1998), the fractional density amplitudes in the fast wind may have been underestimated, and thus the difference between the fast and slow wind may be more pronounced.

The enhancement of the fractional density fluctuation around 6 R_S might explain the change in the power-law characteristics of the phase fluctuation spectrum in this region shown in Fig. 21. The spectrum can be expressed by a single power law below ~6 R_S where turbulence dominates, while the excess power due to acoustic waves below the frequency of 0.5–2 Hz causes the bending structure of the phase fluctuation spectrum beyond ~6 R_S. Since the majority of the waves have frequencies lower than 10^{-2} Hz, the steeper power law on the low frequency side is consistent with the effect of acoustic waves.

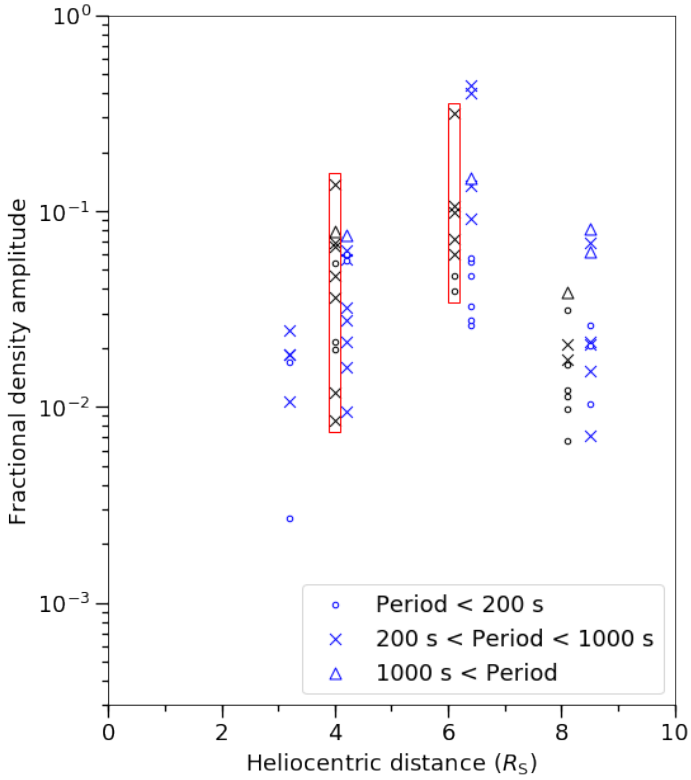

Figure 35. Radial distribution of the fractional density amplitude. The definitions of the symbols are the same as Fig. 34.

Next, assuming that the observed waves are acoustic waves, we estimate the modified wave energy fluxes S_c defined as (Jacques 1997; Suzuki and Inutsuka 2005; Miyamoto et al. 2014):

$$S_c = m_p n_0 v'^2 \frac{(v_s + V)^2}{v_s} \frac{r^2 \mathrm{g}(r)}{r_c^2 \mathrm{g}(r_c)} \tag{13}$$

where m_p is the proton mass, v' is the velocity amplitude of the acoustic wave, which is estimates as $v' = v_s n'/n_0$, $\mathrm{g}(r)$ is a function for the superradial expansion of the flux tube (Kopp and Holzer 1976; Suzuki and Inutsuka 2005), and $r_c = 1.02\ R_S$ is the distance for normalization. Under the condition that no waves are generated and dissipate in the expanding atmosphere, S_c is an adiabatic constant. Since $\mathrm{g}(r)$ takes into account the rapid expansion below ~1.2 R_S and remains unity above ~1.2 R_S, the choice of the superradial expansion factor does not influence the relative radial dependence of the result covering 1.36–9.0 R_S.

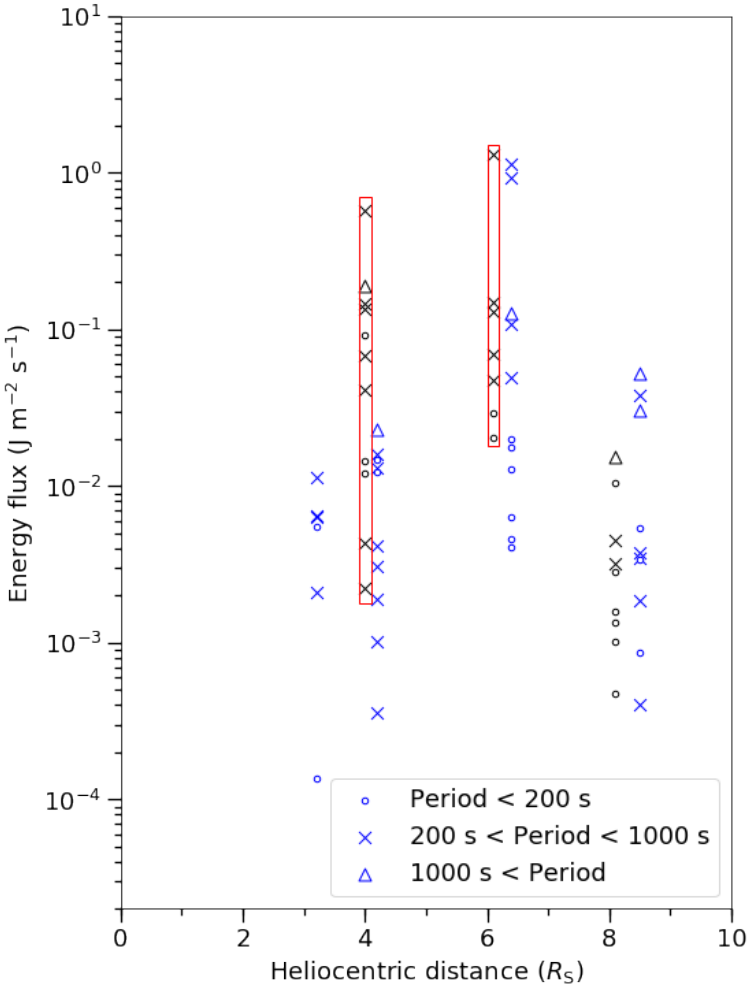

Figure 36. Radial distribution of the wave energy flux. The definitions of the symbols are the same as Fig. 34.

Figure 36 shows the radial distributions of the wave energy flux. The energy flux increases with distance up to ~6 R_S and decays beyond ~6 R_S both on the western and eastern sides. This trend also appeared in the Akatsuki's radio occultation in 2011 (Miyamoto et al. 2014, see Figure 5). If there is no energy injection from the coronal base to the outer corona, the energy flux would not increase with distance. Therefore, this result shows the energy is injected in the outer corona, such as ~6 R_S.

As the periods of the acoustic waves detected by our analysis exceed the acoustic cut-off period in the transition region of 150 s (Erdélyi et al. 2007), these waves cannot have propagated from the photosphere. For these reasons, the radial distributions of the

fractional density amplitude and the wave energy flux imply that Alfvén waves propagating from the photosphere generate acoustic waves in the outer corona and that the generated acoustic waves dissipate to heat the corona as with the result of Miyamoto et al. (2014). We can see the same tendency in both ascending phase (year 2016) and descending phase (year 2016). The maximum energy flux at each distance is also comparable to that in the observation in 2011 (Miyamoto et al. 2014).

The energy fluxes in the fast solar wind originating from the coronal hole around 4 R_S and 6 R_S tend to surpass those from other regions at similar distances, although the difference at ~6 R_S is not large. Considering fast winds have lower density than slow winds (Altschuler et al.1972), the actual energy fluxes in the fast solar wind originating from the coronal hole around 4 R_S and 6 R_S might be larger. This suggests that the fast solar wind originating from the coronal hole is powered by a larger injection of wave energy than the slow wind originating from other regions.

5. Conclusions

Radio occultation observations of the solar corona were conducted by using JAXA's Venus orbiter Akatsuki in 2016. During the observation campaign, the ray path of the radio wave transmitted from Akatsuki crossed both relatively fast winds that will originate from a coronal hole and slow winds from other regions. We have analyzed the time series of the intensity and the phase/frequency of the received radio wave, both of which were derived from the recorded open-loop (voltage time series) data. The results were interpreted in an integrated manner.

Physical parameters (flow velocity, power-law exponent, axial ratio, inner scale, and the magnitude of the power) were retrieved from the intensity scintillation time series by fitting a theoretical spectrum to the observed power spectra. The radial distribution of the derived solar wind velocity clearly showed a difference between the two types of the solar wind (Fig. 18(a)). We also found that the inner scale increases with the heliocentric distance and that the fast solar wind has larger inner scales than the slow solar wind (Fig. 18(b)). This behavior is consistent with the inertial length model both qualitatively and quantitatively, as in Coles and Harmon (1989) and Yamauchi et al. (1998).

We applied wavelet analysis to the frequency time series to detect quasi-periodic fluctuations, that are thought to represent acoustic waves, and quantify the amplitude, the period, and the coherence time of each wave event. The density amplitude and the wave energy flux were also estimated following the method of Miyamoto et al. (2014). We confirmed that the fractional density amplitude increases with distance up to ~6 R_S, then it decays beyond ~6 R_S (Fig. 35). The amplitude reaches tens of percent, suggesting a possibility of wave breaking. The energy flux also increases with distance up to ~6 R_S suggesting local generation of waves, then it decays beyond ~6 R_S (Fig. 36). This tendency, seen in the descending phase of the solar activity cycle (year 2016), is the same as the one seen in the ascending phase in 2011 (Miyamoto e al. 2014). As the periods of acoustic waves detected by our analysis exceed the acoustic cut-off period of the transition region of 150 s, these waves cannot propagate from the photosphere. Therefore, it is probable that the radial distributions of the fractional density amplitude and the energy flux indicate that the Alfvén waves propagating from the photosphere generate acoustic waves in the outer corona, and the generated acoustic waves dissipate to heat the corona, as suggested by Miyamoto et al. (2014).

The phase scintillation spectrum can be expressed by a single power law below ~6 R_S where turbulence dominates, while it cannot be expressed by a single power law and a

bending is seen around the frequency of 0.5–2 Hz beyond ~6 R_S, suggesting an excess power at lower frequencies (Fig. 21). The enhancement of the fractional density amplitude around 6 R_S (Fig.35) might explain such a change in the power-law characteristics of the phase fluctuation spectrum in this region since the majority of the waves have frequencies lower than 10^{-2} Hz.

Furthermore, the energy fluxes in the fast solar wind originating from the coronal hole around 4 R_S and 6 R_S tend to surpass those from other regions at similar distances, although the difference at ~6 R_S is not large. Considering that fast winds have lower densities than slow winds (Altschuler et al. 1972), the actual energy fluxes in the fast solar wind will be larger, and thus the difference between the fast and slow wind may be more pronounced. The results suggest that the fast solar wind originating from the coronal hole is powered by a larger injection of wave energy than the slow wind originating from other regions. The use of different background plasma density models for the fast and slow winds is left for future studies.

In this paper, we only used the data obtained in 2016, which is in a descending phase of the solar activity. Akatsuki has conducted similar observations in various solar activity phases covering from the minimum to the maximum. Comprehensive data processing as conducted in this study should be repeated for other data sets to reveal the dependences on the solar activity.

Acknowledgements

The author would like to thank Professor Takeshi Imamura for unfailing grate supports. His meticulous comments, suggestions and encouragement were an enormous help to the author. Thanks to Professor Munetoshi Tokumaru, Dr. Daiko Shiota, Dr. Hiroki Ando, the members of the Akatsuki project team, the STLE project team, the UDSC operation team, and other members of astrobiology group.

Reference

[1] Altschuler, M.D., Trotter, D.E., and Orrall, F.Q.: 1972, Coronal holes, Sol Phys 26, 354.

[2] Armstrong, R. and Woo, J. W.: 1981, Solar wind motion within 30 R_S: Spacecraft radio scintillation observations, Astron Astrophys,103, 415.

[3] Coles, W.A. and Harmon, J.K.: 1978, Interplanetary scintillation measurements of the electron density power spectrum in the solar wind, J.Geophys.Res., 83, 1413.

[4] Coles, W.A. and Harmon, J.K.: 1989, Propagation observations of the solar wind near the sun, Astrophysical Journal, 337, 1034.

[5] Coles, W.A., Esser, R., Lovhaug, U.P., Markkanen, J.: 1991, Comparison of solar wind velocity measurements with a theoretical acceleration model, J.Geophys.Res., 96, 13849.

[6] Coles, W.A.: 1995, Interplanetary scintillation observations of the high-latitude solar wind, Space Sci. Rev.,72, 211.

[7] Cranmer, R., Adriaan, A., van Ballegooijen, and Edgar, R.J.: 2007, Self-consistent coronal heating and solar wind acceleration from anisotropic magnetohydrodynamic turbulence, Astrophysical Journal, 171, 520.

[8] Cranmer, R.: 2012, Self-consistent models of the solar wind, Space Sci Rev, 172, 145.

[9] Cranmer, R. and Winebarger, A.R.: 2019, The properties of the solar corona and its connection to the sun, Annual Review of Astronomy Astrophysics, 57, 157.

[10] Dulk, G.A., McLean, D.J.: 1978, Coronal magnetic fields, Sol Phys, 57, 279.

[11] Efimov, A.I.: 1994, Radial profile measurements of the solar wind speed using radio sounding techniques, Space Science Reviews, 70, 397.

[12] Efimov, A. I., Lukanina, L. A., Samoznaev, L. N., Rudash, V. K., Chashei, I. V., Bird, M. K., Pätzold, M., Tellmann, S.: 2010, Quasi-periodic fluctuation detected in Mars Express coronal radio sounding observations, API-CP, 1216, 90.

[13] Efimov, A. I., Lukanina, L. A., Samoznaev, L. N., Rudash, V. K., Chashei, I. V., Bird, M. K., Pätzold, M., Tellmann, S., The MEX, VEX, ROS Radio Science Team: 2012, Quasiperiodic frequency fluctuations observed during coronal radio sounding experiments 1991-2009, Advances in Space Research, 49, 500.

[14] Erdélyi, R., Malins, C., Téth, G., and Pontieu, B.De.: 2007, Leakage of photospheric acoustic waves into non-magnetic solar atmosphere, Astron Astrophys, 467, 1299.

[15] Imamura, T., Noguchi, K., Nabatov, A., Oyama K.-I., Yamamoto, Z., and Tokumaru, M.: 2005, Phase scintillation observation during coronal sounding

experiments with NOZOMI Spacecraft, Astron Astrophys, 439, 1165.
[16] Imamura, T., Iwata, T., Yamamoto, Z., Mochizuki, N., Kono, Y., Matsuno, K., Liu, Q., Noda, H., Hanada, H., Oyama, K., Nabatov, A., Futaana, Y., Saito, A., Ando, H.: 2010, Studying the Lunar Ionosphere with SELENE Radio Science Experiment, Space Science Reviews, 154, 305.
[17] Imamura, T., Toda. T, Tomiki, A., Hirahara, D., Hayashiyama, T., Mochizuki, N., Yamamoto, Z., Abe, T., Iwata, T., Noda, H., Futaana, Y., Ando, H., Häusler, B., Pätzold, M., and Nabatov, A.: 2011, Radio occultation experiment of the Venus atmosphere and ionosphere with the Venus orbit Akatsuki, Earth Planets Space, 63, 493.
[18] Imamura, T., Tokumaru, M., Isobe, H., Shiota, D., Ando, H., Miyamoto, M., Toda, T., Häusler, B., Pätzold, M., Nabatov, A., Asai, A., Yaji, K., Yamada, M., Nakamura M.: 2014, Out flow structure of the quiet sun probed by spacecraft radio scintillations in strong scattering, Astrophysical Journal, 788, 117.
[19] Imamura, T., et al.: 2017, Initial performance of the radio occultation experiment in the Venus orbiter mission Akatsuki, Earth Planets Space, 69, 137.
[20] Jacques, S. A.: 1977, Momentum and energy transport by waves in the solar atmosphere and solar wind., Astrophysical Journal, 215, 942.
[21] Kopp, R. A., and Holzer, T. E.: 1976, Dynamics of coronal hole, Sol Phys, 49, 43.
[22] Lipa, B., and Tyler, L: 1979, Statistical and computational uncertainties in atmosphere profiles from radio occultation: mariner 10 at Venus, Icarus, 39, 192.
[23] Matsumoto, T., Suzuki, T.: 2012, Connecting the sun and the solar wind: the first 2.5 dimensional self-consistent MHD simulation under the Alfvén wave scenario, Astrophysical Journal, 749, 8.
[24] McComas, D.J., Ebert, R.W., Elliott, H.A., Goldstein, B.E., Gosling, J.T., Schwadron, N. A., and Skoug, R.M.: 2008, Weaker solar wind from the polar coronal holes and the whole sun, Geophys Res Lett, 35, 18103.
[25] Miyamoto, M., Imamura, T., Tokumaru, M., Ando, H., Isobe, H., Asai, A., Shiota, D., Toda, T., Häusler, B., Pätzold, M., Nabatov, A., Nakamura, M.: 2014, Radial distribution of compressive waves in the solar corona revealed by Akatsuki radio occultation observations, Astrophysical Journal, 797, 51.
[26] Parker, E., N.: 1959, Dynamics of the interplanetary gas and magnetic fields, Astrophysical Journal, 128, 664.
[27] Pätzold, M., Bird, M. K., Volland, H., Levy, G. S., Seidel, B. L. and Stelzried, C. T.: 1987, The mean coronal magnetic field determined from Helios faraday rotation measurement, Sol Phys, 109, 91.

[28] Pätzold, M., Karl, J., and Bird, M. K.: 1996, Coronal radio sounding with Ulysses: dual-frequency phase scintillation spectra in coronal holes and streamers, Astron Astrophys, 316, 449.

[29] Raja, K.S., Subramanian2, P., Ingale2, M. and Ramesh, R.: 2019, Dissipation scale lengths of solar wind turbulence, Astrophysical Journal, 872, 77.

[30] Scott, S.L., Coles, W.A. and Bourgois, G.: 1983, Solar wind observations near the Sun using interplanetary scintillation, Astron Astrophys., 123, 207.

[31] Shoda, M., Yokoyama, T., and Suzuki, T.K. 2018, Frequency-dependent Alfvén-wave propagation in the solar wind: onset and suppression of parametric decay instability, Astrophysical Journal, 860, 17.

[32] Shoda, M., Suzuki, T.K., Mahboubeh, A.T. and Yokoyama, T.: 2019, Three-dimensional simulation of the fast solar wind driven by compressible magnetohydrodynamic turbulence, Astrophysical Journal, 880, 2.

[33] Suzuki, T. and Inutsuka, S.: 2005, Making the corona and the first solar wind: a self-consistent simulation for the low-frequency Alfvén waves from the photosphere to 0.3 AU, Astrophysical Journal, 632, 49.

[34] Tokumaru, M., Mori, H., Tanaka, T., Kondo, T., Takaba, H. and Koyama, Y.: 1991, Solar wind near the sun observed with interplanetary scintillation using three microwave frequencies, J.Geomag.Geoelectr., 43, 619.

[35] Tokumaru, M., Mori, H., Tanaka, T. and Kondo, T.: 1995, Evolution of the solar wind structure in the acceleration region during 1990-1993 (STEP interval), J.Geomag.Geoelectr., 47, 1113.

[36] Torrence, C. and Compo, G.P.: 1998, A practical guide to wavelet analysis. Bulletin of the American Meteorological Society, Amer. Meteor. Soc., 79, 61.

[37] Withbroe, G. L., and Noyes, R. W.: 1977, Mass and energy flow in the solar chromosphere and corona, Ann. Rev. Astron Astrophys., 15, 363.

[38] Woo, R. and Armstrong, J. W.: 1979, Spacecraft radio scattering observations of the power spectrum of electron density fluctuations in the solar wind, Geophysical Research, 84, 7288.

[39] Yamauchi, Y., Tokumaru, M., Kojima, K., Manoharan, P.K., Esser, R.: 1998, A study of density fluctuations in the solar wind acceleration region, J.Geophys.Res, 103, 6571.